「卒業論文」

Analysis of Island-trapped Waves off the Izu-Islands

（伊豆諸島において島に捕捉された流れに関する考察）

「平成 26 年 2 月」

03-120864

Faculty of Engineering, Department of Systems Innovation

Takaya Uchida

SUPERVISOR

Professor Takuji Waseda

ABSTRACT

Analysis of island-trapped waves has been made off the Izu-Islands, particularly around the Miyake Island and the Hachijo Island. The ITWs were observed in reanalysis data of current velocity, sea-surface elevation, temperature and salinity provided by the Japan Agency for Marine-Earth Science and Technology (JAMSTEC). From Fourier analysis and cross-spectral analysis, we determined that the ITWs have periods close to the K1, P1, O1 and Q1 tidal constituents, which are longer than the inertial period in that region. We have also found, from Complex Empirical Orthogonal Function analysis of the horizontal velocity, that the observed ITWs had horizontal and vertical modal structures. It is likely that the islands have resonant modes whose periods lie in the vicinity of the diurnal tidal components and that the ITWs are forced by internal tides. We will clarify this by comparing the analyzed results of the reanalysis data with the island-trapped wave theory, and numerical simulations with ideal topography using the Princeton Ocean Model.

DECLARATION

I confirm that this is my own work and the uses of all material from other sources have been fully and properly acknowledged.

Takaya Uchida

ACKNOWLEDGEMENTS

TABLE OF CONTENTS

1. Introduction

There has been much progress in research about trapped waves along a straight coast line both theoretically and numerically (e.g. Huthnance[13] (1978), Clarke[12] (1977)). For straight coast lines, the dispersion relations of the trapped waves are continuous. When the coast line is closed such as an island, however, the lack of a large-scale characteristic length restricts the simplification of the governing equations for trapped waves and the dispersion relations exist discretely with an additional quantized azimuthal mode number. This leads to a resonant system allowing discrete spectra of island-trapped wave (ITW) modes. It was stated by Longuet-Higgins[1] (1969) that complete trapping of the ITWs only occur at frequencies lower than the inertial frequency, so in this study, we will only focus on frequencies lower than the inertial frequency in the Izu region which corresponds to somewhere around 21.5 hours in period.

Observational evidence of wind-driven subinertial ITWs have been provided around the Oahu Island (e.g. Miyata and Groves[14] (1968), Miyata[15] (1993), Longuet-Higgins[3] (1971)), and the Bermuda Island (e.g. Wunsch[4] (1972), Hogg[5] (1980) and Brink[6] (1999)). Miyata and Groves (1968) reported on a 48 hour spectral peak of temperature variation. Longuet-Higgins (1971) and Miyata (1993) both made an attempt to explain the observed 48 hour peak around the Oahu Island. While Longuet-Higgins (1971) provided no explicit reason about choosing the values of the parameters which he used, Miyata (1993) clarified that the 48 hour period cohered with the period of the ITWs which had the smallest wavenumber in his theoretical model. Therefore, the results given by Miyata (1993) may be more convincing in clarifying that the spectral peak was caused by ITW modes. Wunsch (1972) and Hogg (1980) also report spectral peaks of temperature variation corresponding to 38 hours and 26.1 hours respectively and they both give comprehensive conclusions that the observed temperature variations were caused by ITW modes. Although the 26.1 hour peak lies in the vicinity of the K1, P1, O1 and Q1 tidal component, Hogg (1980) has provided cogent evidence of seasonality, and hence concluded that the ITWs were excited by wind.

In this paper, we report on currents circulating clockwise around the Izu-Islands, particularly the Miyake Island and the Hachijo Island, observed in reanalysis data of current velocity, sea-surface elevation, temperature and salinity, provided by the Japan Agency for Marine-Earth Science and Technology (JAMSTEC) (Sil et al.[18] 2013 IWMO). We believe that the circulating currents represent ITWs and as we will see in the main discussion that the eigenperiods of the ITWs have close values to the diurnal tidal components under the conditions around the Miyake Island, hence indicating the possibility of tidal forcing. Although theory suggests that ITWs are expected to exist around any island except for regions close to the equator where the inertial frequency reduces to zero, ITWs with diurnal periods are limited to

regions with latitudes north of 30°N. The latitude of the Izu region is around 34°N, which meets this requirement and we believe that this is the first paper to identify tidal-driven ITWs.

Methods and results of data analysis will be provided in the next section. In Section 3, the ITW theory will be reviewed and expanded aiming to explain the currents observed in the reanalysis data. Conditions and results of the numerical simulation using the Princeton Ocean Model (POM) will be given in section 4 and conclusions will be given in section 5.

2. Data Analysis

The source of data which we looked into was reanalysis data of current velocity, sea-surface elevation, temperature and salinity provided by JAMSTEC (Sil et al. 2013 IWMO). The model used in computing the data assimilation was the Stony Brook Parallel Model (Jordi and Wang[17] (2012)) (hereafter we will refer to the reanalysis data as sbPOM) and was nested into another reanalysis data JCOPE2 which had a coarser horizontal resolution of 3 km. The region of sbPOM was taken as $136° \sim 142°E$, $30° \sim 36°N$ and the horizontal resolution was 1 km. The sea-surface fluxes were provided from NCEP reanalysis data every 6 hours and the lateral boundary conditions were satisfied by the JCOPE2 and the tidal model NAO99. The duration of the data was from July 1, 2011 until December 1, 2012. We have focused on the Miyake Island and the Hachijo Island because these two islands are relatively large among the islands consisting the Izu-Islands and far away from the other islands. Particularly, the configuration of the Miyake Island is rather circular than the Bermuda Island (Wunsch (1972)), hence, allowing us to apply the ITW theory of a cylindrical island to a better extent. Although the period of the reanalysis data was longer than a year, we were only able to identify the circulating currents around the Miyake Island in March and May and around the Hachijo Island in December. We will, therefore, only consider data in March 2012 for the Miyake Island and December 2011 for the Hachijo Island where the circulating currents were present throughout the whole month. The distribution of horizontal velocity around the Miyake Island at depth 0 m on March 6, 2012 is shown in Fig. 1. The patterns representing the circulating currents seem to circle clockwise around the island in a day, indicating a period of approximately 24 hours.
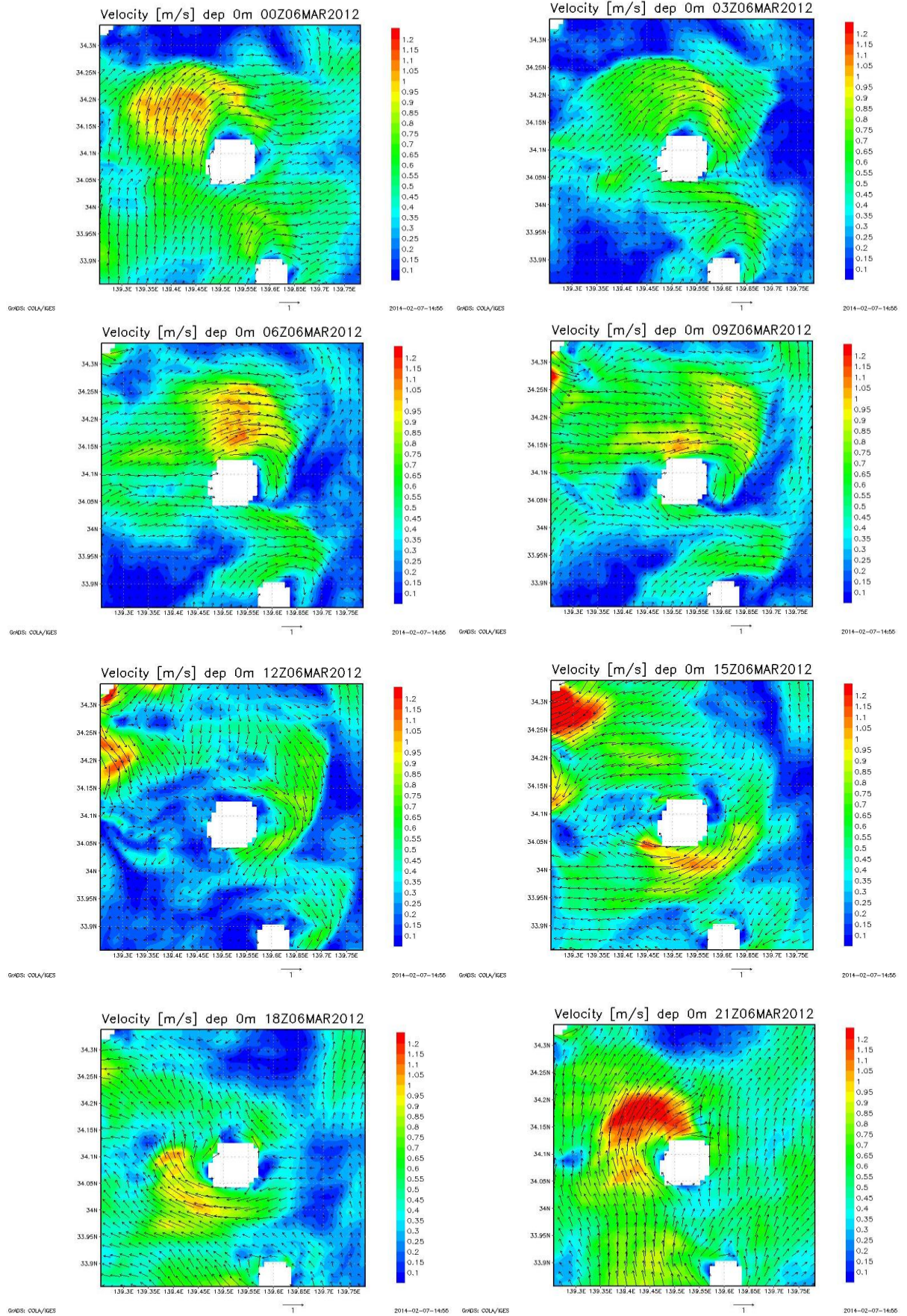
Figure 1. Temporal transition of the distribution of horizontal velocity on March 6, 2012. The figures represent the magnitude of the horizontal velocity and velocity vectors every three hours.

2.1. Hopf-Mellor diagram

In order to determine the presence of currents progressing around the islands, we created Hopf-Mellor diagrams (Fig. 3, Fig. 4) of the magnitude of baroclinic horizontal velocity at depth 0 m and sea-surface elevation. Fig. 2 represents the topography in meters around each island along with the path of each Hopf-Mellor diagram. The diagonal patterns in the Hopf-Mellor diagrams of horizontal velocity indicate the existence of a progressive wave circulating around both islands whereas the Hopf-Mellor diagrams of sea-surface elevation around Miyake Island show only horizontal patterns (Fig. 3). Comparing the Hopf-Mellor diagrams of horizontal velocity and sea-surface elevation, we see that there are no propagating signals circulating the islands for sea-surface elevation, especially for the Miyake Island, indicating that the currents are internal modes. The currents around the Hachijo Island seem to be a superposition of external and internal modes since, in the Hopf-Mellor diagram of sea-surface elevation, a diagonal pattern along with a horizontal pattern can be observed (Fig. 4).
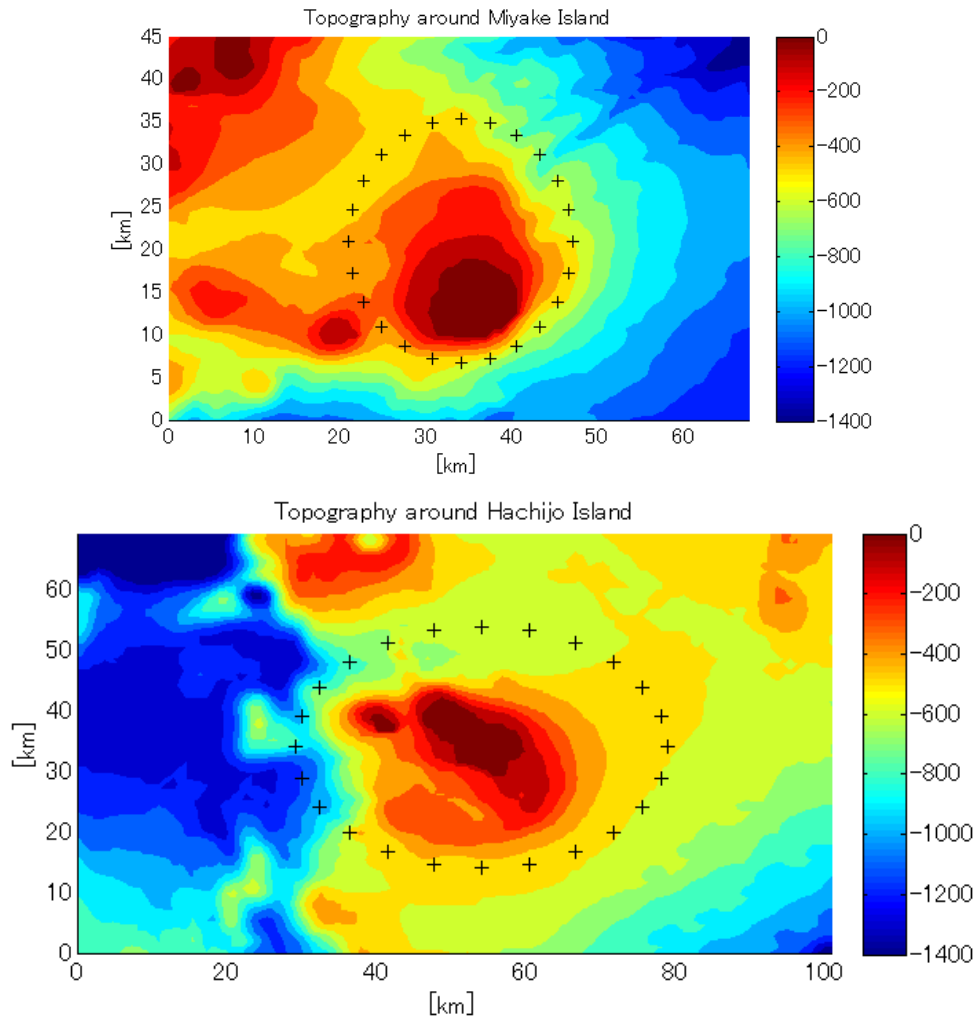
Figure 2. The + marks represent the points at which data was taken to create the Hopf-Mellor diagrams. 0 degrees was taken at the northern limit of the path and the positive direction of the angle was taken clockwise. The color bar represents the topography in meters.
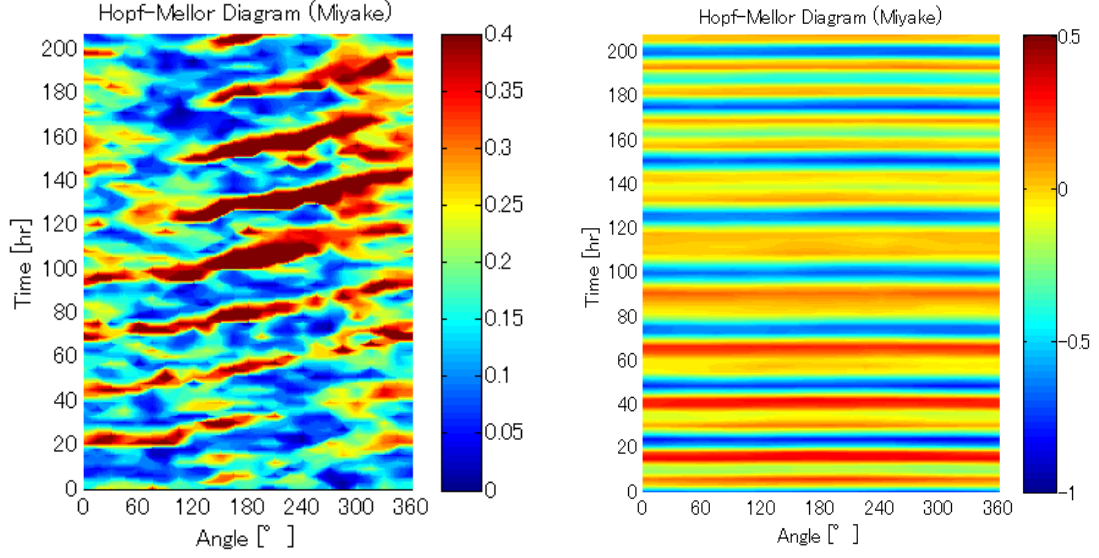

Figure 3. Hopf-Mellor diagram of horizontal velocity (left) and sea-surface elevation (right) around the Miyake Island taken on the path shown in Fig. 1. The color bar represent horizontal velocity in m/s and sea-surface elevation in meters.
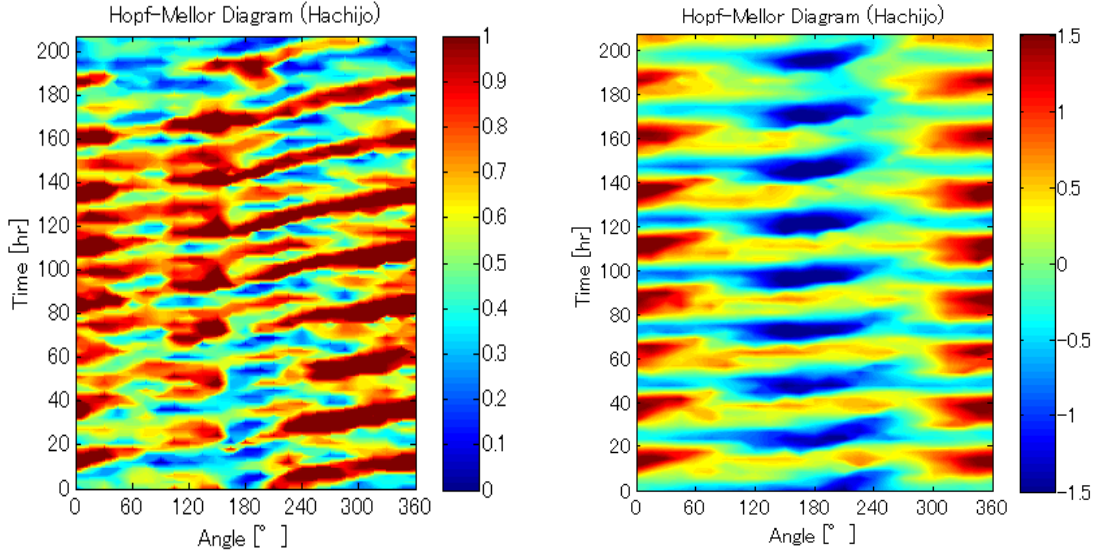
Figure 4. Hopf-Mellor diagram of horizontal velocity (left) and sea-surface elevation (right) around the Hachijo Island taken on the path shown in Fig. 1. The color bar represent horizontal velocity in m/s and sea-surface elevation in meters.

2.2. EOF/CEOF analysis

We conducted an Empirical Orthogonal Function (EOF) analysis and Complex Empirical Orthogonal Function (CEOF) Analysis of horizontal velocity in order to identify modes circulating around Miyake Island. EOF analysis is a method to find the principle components x that best explain the variance of the domain. We shall put the data of horizontal velocity

$$\mathbf{V} = \begin{bmatrix} u_1^1 & \cdots & u_1^N \, v_1^1 & \cdots & v_1^N \\ \vdots & \ddots & \vdots \quad \vdots & \ddots & \vdots \\ u_M^1 & \cdots & u_M^N \, v_M^1 & \cdots & v_M^N \end{bmatrix} \tag{1}$$

The covariance matrix can be written as:

$$\mathbf{\Sigma} = \frac{1}{N-1} \mathbf{V}^{\mathrm{T}} \mathbf{V} \tag{2}$$

Therefore, when the eigenvalue corresponding to $\boldsymbol{x}$ is λ, the eigenvalue problem becomes:

$$\mathbf{\Sigma}\boldsymbol{x} = \lambda\boldsymbol{x} \tag{3}.$$

Assuming that $\boldsymbol{x}$ is unitary, λ can be calculated from

$$\lambda = \boldsymbol{x}^{\mathrm{T}}\mathbf{\Sigma}\boldsymbol{x} \tag{4}$$

which reduces the problem to deriving $\boldsymbol{x}$ that maximizes the value $\boldsymbol{x}^{\mathrm{T}}\mathbf{\Sigma}\boldsymbol{x}$. The results of $\boldsymbol{x}_1$, $\boldsymbol{x}_2$, $\boldsymbol{x}_3$ and $\boldsymbol{x}_4$ are shown in Fig. 5.

Figure 5. EOF mode of horizontal velocity at depth 0 m. The color bar represents the magnitude of horizontal velocity in m/s. The magnitude of the velocity vectors is preserved.

In addition, we conducted a CEOF analysis in order to identify propagating modes. This method is a straightforward expansion of the EOF analysis to complex variables. Putting the Hilbert transform of $\mathbf{V}$ as $\widehat{\mathbf{V}}$ and constructing a complex state matrix:

$$\mathbf{Z} = \mathbf{V} + i\hat{\mathbf{V}} \tag{5}$$

The covariance matrix is given as:

$$\Sigma = \frac{1}{N-1}\mathbf{Z}^{\mathrm{T}}\mathbf{Z} \tag{6}$$

and the same steps are taken as in the EOF analysis. If the modes are propagating, the relation between EOF analysis and CEOF analysis is

$$x_i^{\mathrm{EOF}} \sim \mathrm{Re}\big[x_i^{\mathrm{CEOF}}\big], \qquad x_{i+1}^{\mathrm{EOF}} \sim \mathrm{Im}\big[x_i^{\mathrm{CEOF}}\big] \tag{7}$$

The results of x_1, x_2 and x_3 by taking the real parts are shown in Fig. 6. Fig. 5 and Fig. 6 indicate that the currents have horizontal modes and particularly, the results of CEOF analysis imply the existence of progressing current patterns around the Miyake Island.
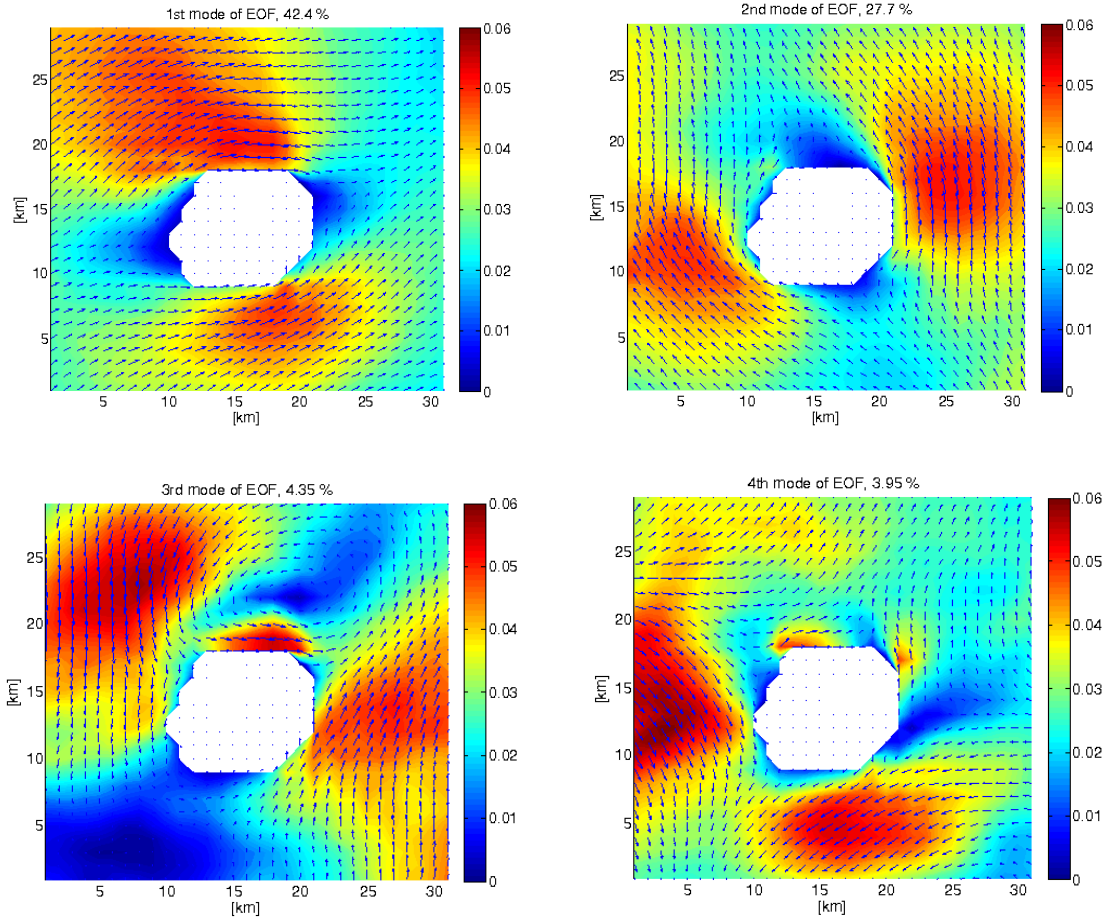

Figure 6. CEOF mode of horizontal velocity at depth 0 m. The color bar represents the magnitude of horizontal velocity in m/s. The magnitude of the velocity vectors is preserved.

We shall further expand the CEOF analysis to three dimensions (Fig. 7) in order to identify horizontal modes and vertical modes. Fig. 7 shows that the circulating currents not only have horizontal modes but also vertical modes and the horizontal mode and vertical mode progress around the Miyake Island as a set.

7

The horizontal modes correspond fairly well with the horizontal modes derived from the two-dimensional CEOF analysis. Looking into the vertical modes, we see that the magnitude of horizontal velocity has large values from the sea surface until 100 m depth and small values close to zero below 100 m depth. The vertical profiles of horizontal velocity seems homologous with the baroclinic 1st mode, implying that the circulating currents are baroclinic. Restricting our discussion to interpreting the vertical component of the 3rd CEOF mode, it seems that the baroclinic 2nd mode is being excited as well on the left side of the island.
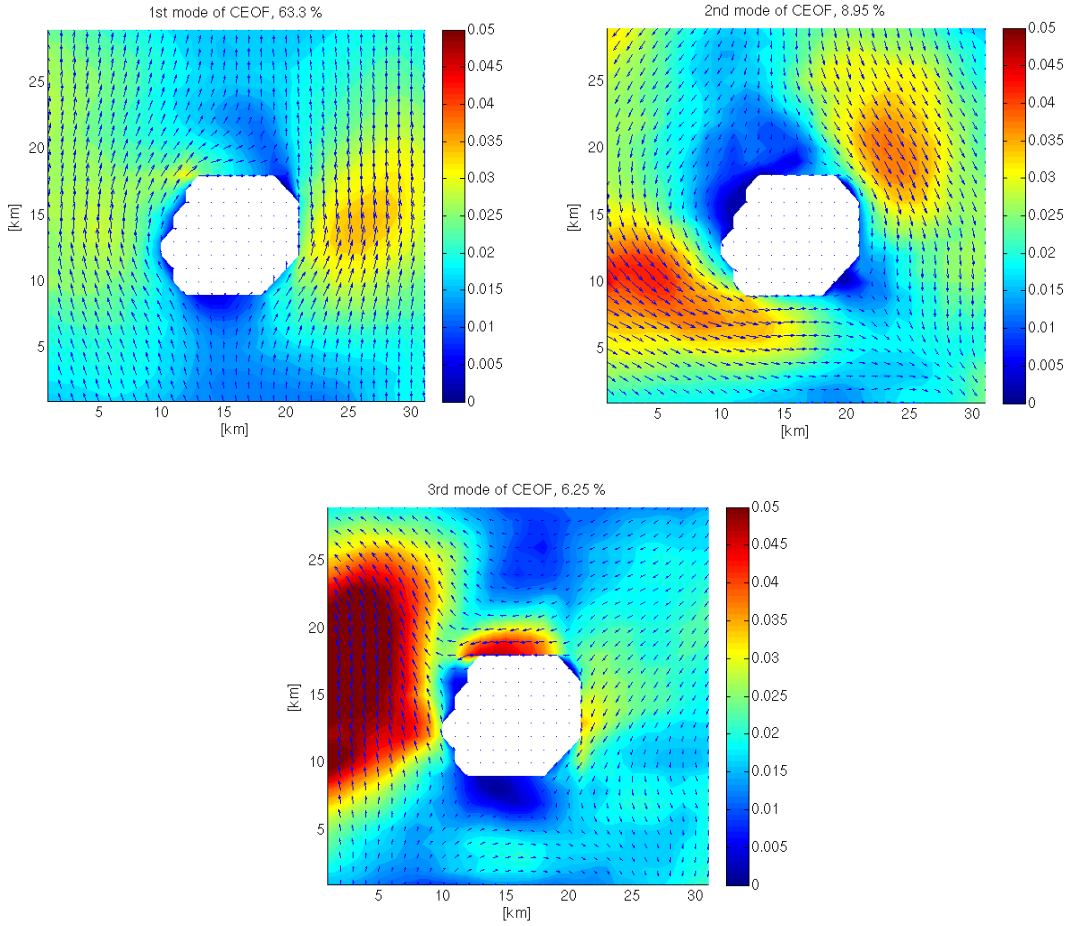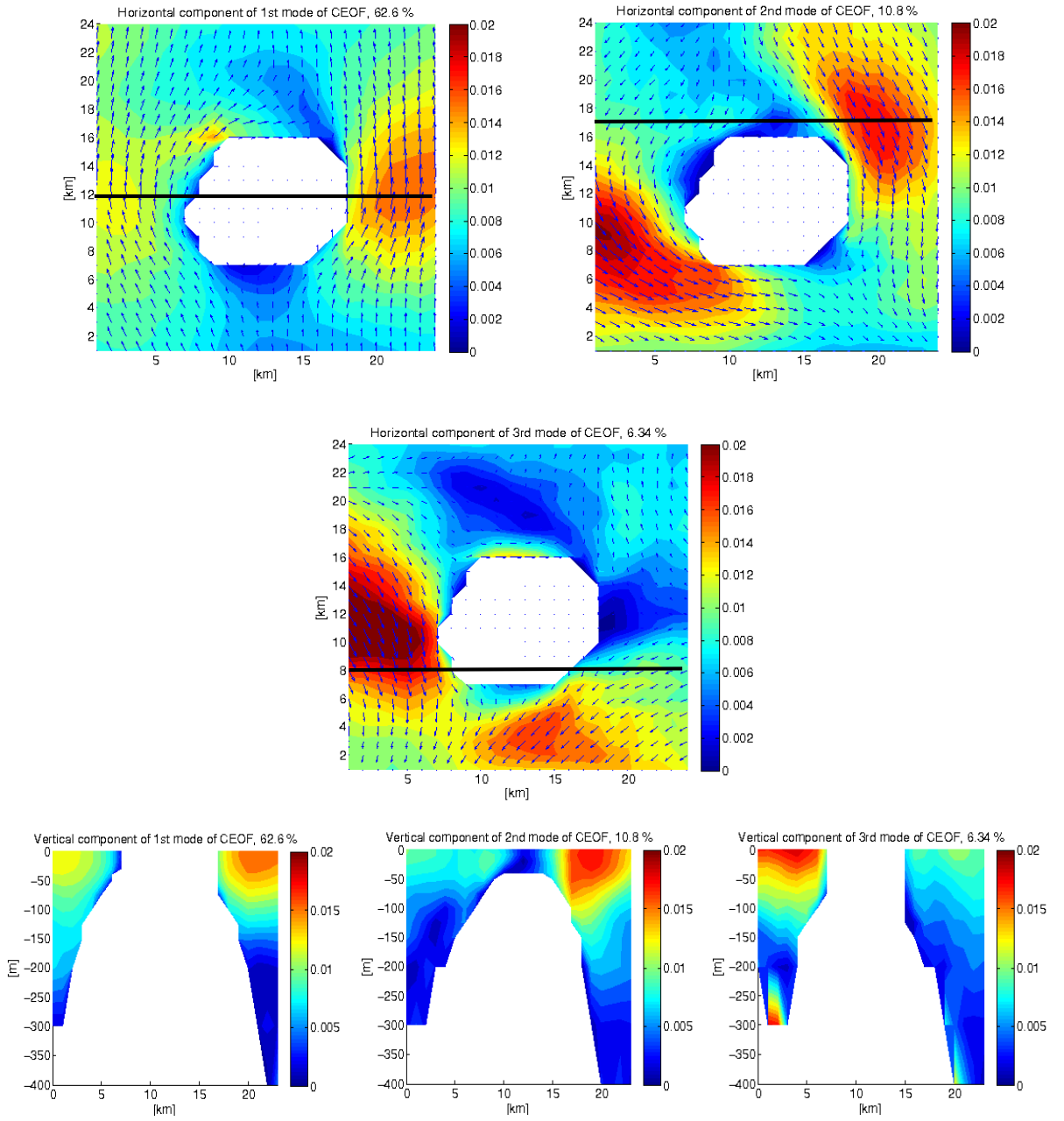
Figure 7. CEOF mode of horizontal velocity at depth 0 m and cross section of horizontal velocity. The color bar represents the magnitude of horizontal velocity in m/s. The magnitude of the velocity vectors is preserved. The black lines indicate where the cross section of the CEOF modes were taken.

For this case, we have also derived the principle component corresponding to each CEOF mode (Fig. 8). While the CEOF modes represent the time average of the signals, the principle component shows the spatial average of the region, which gives us a rough estimate of the time cycle of each CEOF mode. Using the same signs as above, $\mathbf{Z}$ can be decomposed into

$$\mathbf{Z} = \mathbf{TX}^{\mathrm{T}} \tag{8}$$

where $\mathbf{X}$ stands for the CEOF mode matrix, and $\mathbf{T}$ for the principle component matrix. Since the column vectors of $\mathbf{X}$ are normalized and orthogonal to each other $\mathbf{X}$ is unitary, hence:

$$\mathbf{T} = \mathbf{TX}^{\mathrm{T}}\mathbf{X} = \mathbf{ZX} \tag{9}$$

We see from Fig. 8 that the 1st CEOF mode have the time cycle around 24 hours whereas the time cycle of the 2nd and 3rd mode look like a superposition of 24 hours and 12 hours.
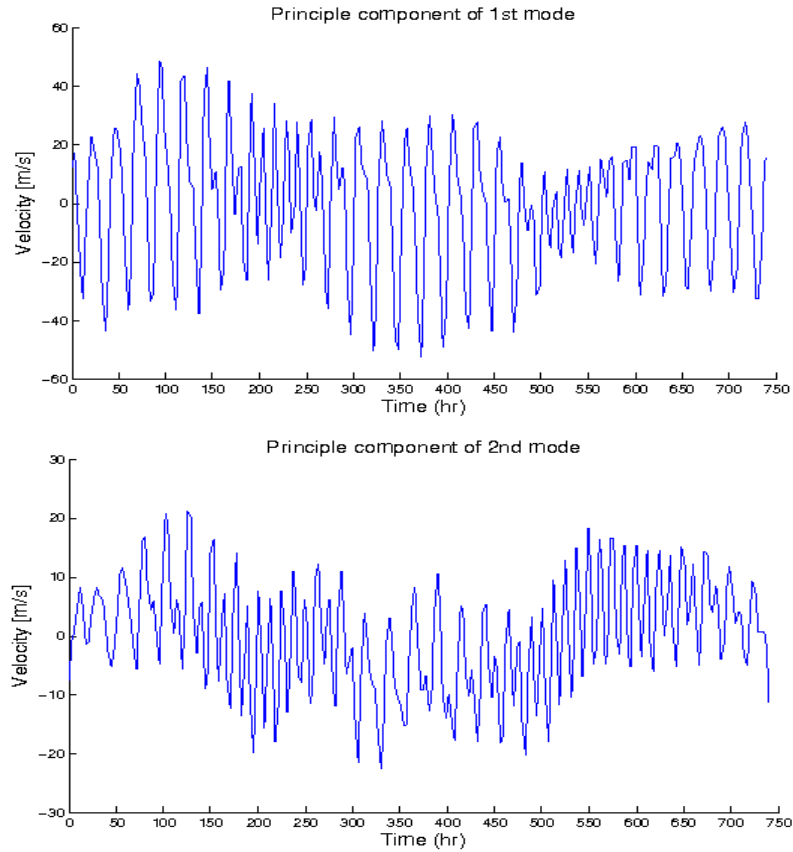
Figure 8. Principle Component of the 1st, 2nd and 3rd CEOF three dimensional mode.

2.3. Fourier and cross-spectral analysis

From visual inspection of the Hopf-Mellor diagrams (Fig. 3, 4), the ITWs seem to have periods around 24 hours so we will clarify this by using Fourier analysis and cross-spectral analysis. The Fourier analysis for U, east-west component of horizontal velocity and V, north-south component of horizontal velocity were taken at the northern and southern limit, and eastern and western limit respectively of the path taken to create the Hopf-Mellor diagrams.

The length of the time series was taken as 1 month, December for Hachijo Island and March for Miyake Island. The interval between each time step was 3 hours for the reanalysis data and each sample length was taken as 200 steps ($= 200 \times 3 = 600$ hours), which were zero-patted to 256 ($= 2^8$) steps to conduct Fast Fourier Transformation. We will show the results of the Fourier Transformation below in Fig. 9 and Fig. 10.
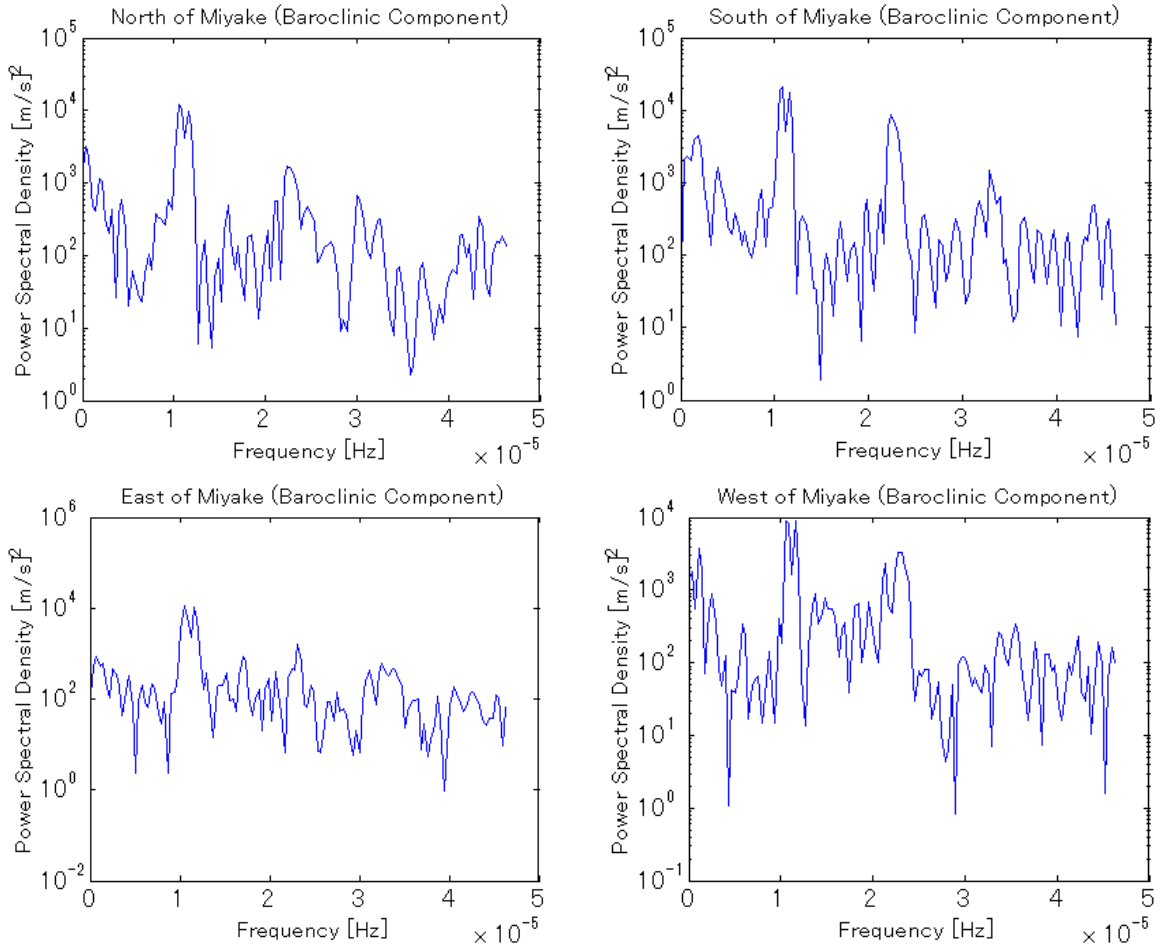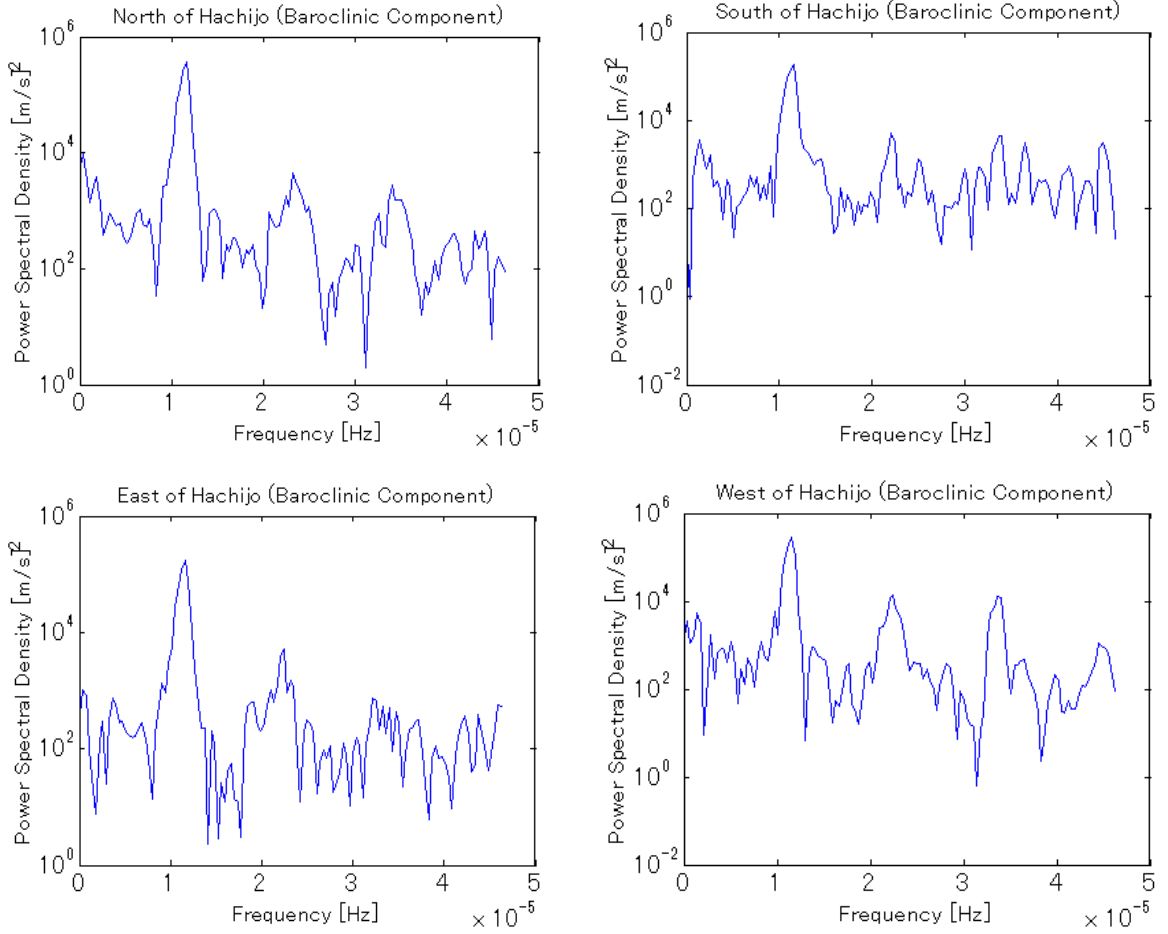
Figure 10. Fourier analysis of baroclinic horizontal velocity around Hachijo Island at the Northern, Southern, Eastern and Western limit of the path shown in Fig. 2.

We will only focus on periods longer than the inertial period where true trapping of the ITWs occurs, as mentioned by Longuet-Higgins (1969) (hereafter L-H). For Miyake Island (Fig. 9), the first, second and third largest peak correspond to 26.48 hours $(= T_M)$, 25.60 hours $(= T_{M'})$ and 24.01 hours $(= T_H)$ where the inertial period was taken as 21.42 hours. As for Hachijo Island (Fig. 10), the largest peak corresponds to T_H, where the inertial period was taken as 21.97 hours. The periods of the diurnal tidal components are T_{K1} (23.93 hours), T_{P1} (24.07 hours), T_{O1} (25.82 hours) and T_{Q1} (26.87 hours). Since the fundamental frequency was $3.617 \times 10^{-7}\ Hz\ (= 1/(256 \times 3)\ hr^{-1})$, the ratio of the difference between periods and fundamental frequency δf are:

$$\frac{\left(\frac{1}{T_{K1}} - \frac{1}{T_H}\right)}{\delta f} = 0.11$$

$$\frac{\left(\frac{1}{T_H} - \frac{1}{T_{P1}}\right)}{\delta f} = 0.080$$

$$\frac{\left(\frac{1}{T_{Q1}} - \frac{1}{T_M}\right)}{\delta f} = 0.42$$

$$\frac{\left(\frac{1}{T_{O1}} - \frac{1}{T_{M'}}\right)}{\delta f} = 0.26$$

All of the values are less than unity and considering the energy leakage, we cannot distinguish the periods of spectrum peaks; T_M, $T_{M'}$ and T_H from the periods of the tidal components. This makes it difficult for us to tell whether we are simply picking up the signals of the tidal components or signals of the currents circulating around the islands. We will therefore look at the results of the phase difference of each frequency between two points on the path shown in Fig. 2 in order to confirm that the velocity components corresponding to each frequency have components progressing around the islands. This can be done by the method below:

$$\Delta\theta = Arg[F(u_1)F^*(u_2)] = Arg\left[\tilde{u}_1\tilde{u}_2 e^{i(\theta_1 - \theta_2)}\right]$$

$$= k_\theta \Delta s = \frac{\sigma}{c}\Delta s = 2\pi f \frac{\Delta s}{c}; \quad \Delta s: \text{path length} \qquad (10)$$

$$\therefore \ \Delta T = \frac{\Delta\theta}{2\pi f}$$

and we get

$$c = \frac{\Delta s}{\Delta T} \quad : \text{phase speed} \qquad (11)$$

In order to minimize the statistical uncertainty, we took an ensemble mean of 11 segments and the phase speed was derived from the Fourier Transformation of the horizontal velocity components U and V.

It should be kept in mind, however, that Fig. 11 may include large errors. While the path length Δs should be taken as the path of the progressing waves, it was derived from the path of the Hopf-Mellor diagram in Fig. 2 and, therefore, Fig. 11 should be treated somewhat as a criteria in determining that the currents corresponding to each frequency have phase speeds. The possible errors do not, however, undermine the fact that the circulating currents have periods lying in the vicinity of the K1, P1, O1 and Q1 tidal component. Considering that that the currents were internal modes, observed throughout a whole month, and that they have periods close to the diurnal tidal components, it is convincing that these currents are tidal driven, and as from the results of harmonic analysis mentioned below, internal tides.

In our harmonic analysis, we used 8 tidal components; K1, P1, O1 and Q1 representing the diurnal tidal component and M2, S2, K2 and N2 representing the semidiurnal tidal component and took the least-square method in determining the amplitude of each component. Comparing

the harmonic analysis of sea-surface elevation and east-west horizontal velocity in the Izu region (Fig. 12), the relative magnitude of the amplitude between semidiurnal tidal frequencies and diurnal tidal frequencies reverses. In other words, the M2 signal is predominant for sea-surface elevation while K1, P1 and O1 signals dominate over the M2 signal for horizontal velocity, indicating that internal tides are being generated at the Izu-Ridge (e.g. Ohwaki et al.[7, 8] (1991, 1994)). Since the currents had periods close to the diurnal tides instead of M2, it is natural to think that the currents are forced by internal tides.
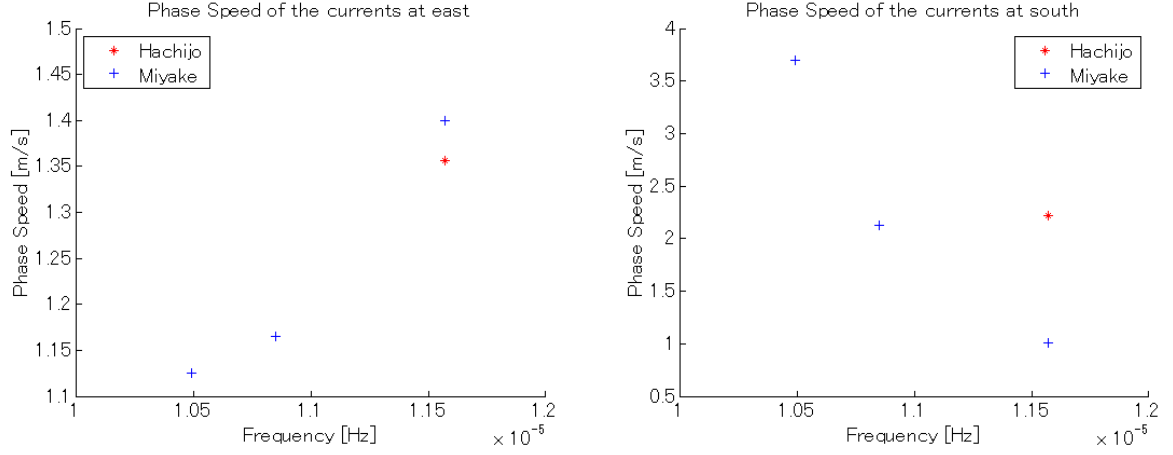
Figure 11. Phase speed of the waves circulating around each island against frequency. We see that the components corresponding to T_H, T_M and $T_{M'}$ in periods have phase speeds.

Figure 12. The amplitude of each tidal component. Elevation is the sea-surface elevation and u stands for the east-west horizontal velocity component. The M2 signal prevails over the other tidal components for elevation but the diurnal signals dominate over the M2 signal for u.

Continuation of Figure 12.

15

Continuation of Figure 12.

3. Island-trapped wave theory

3.1. Derivation of the island-trapped wave theory

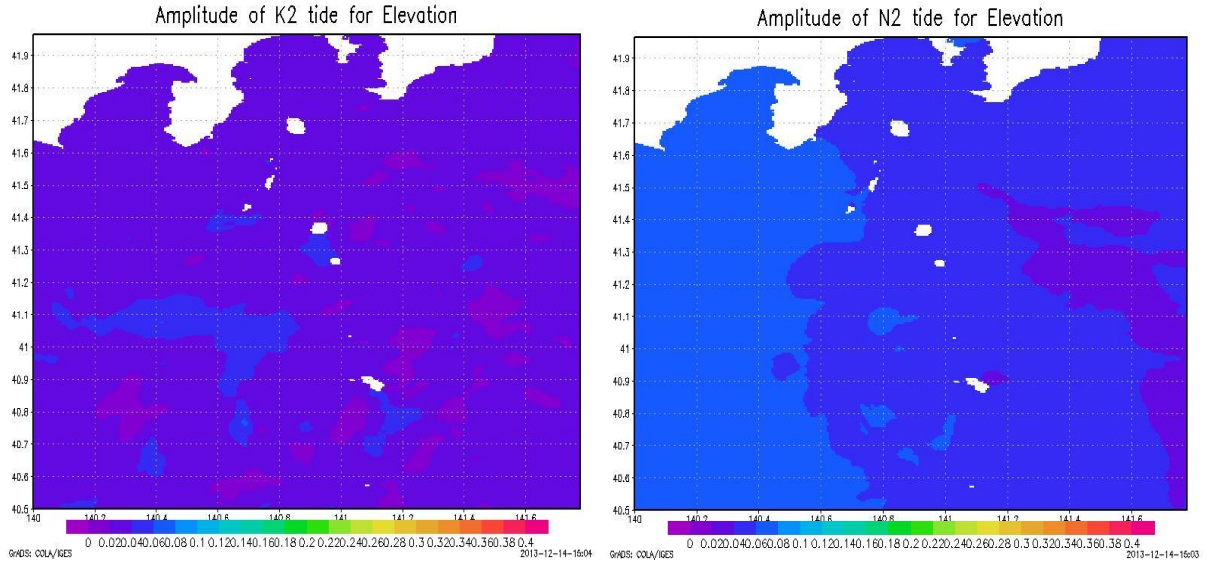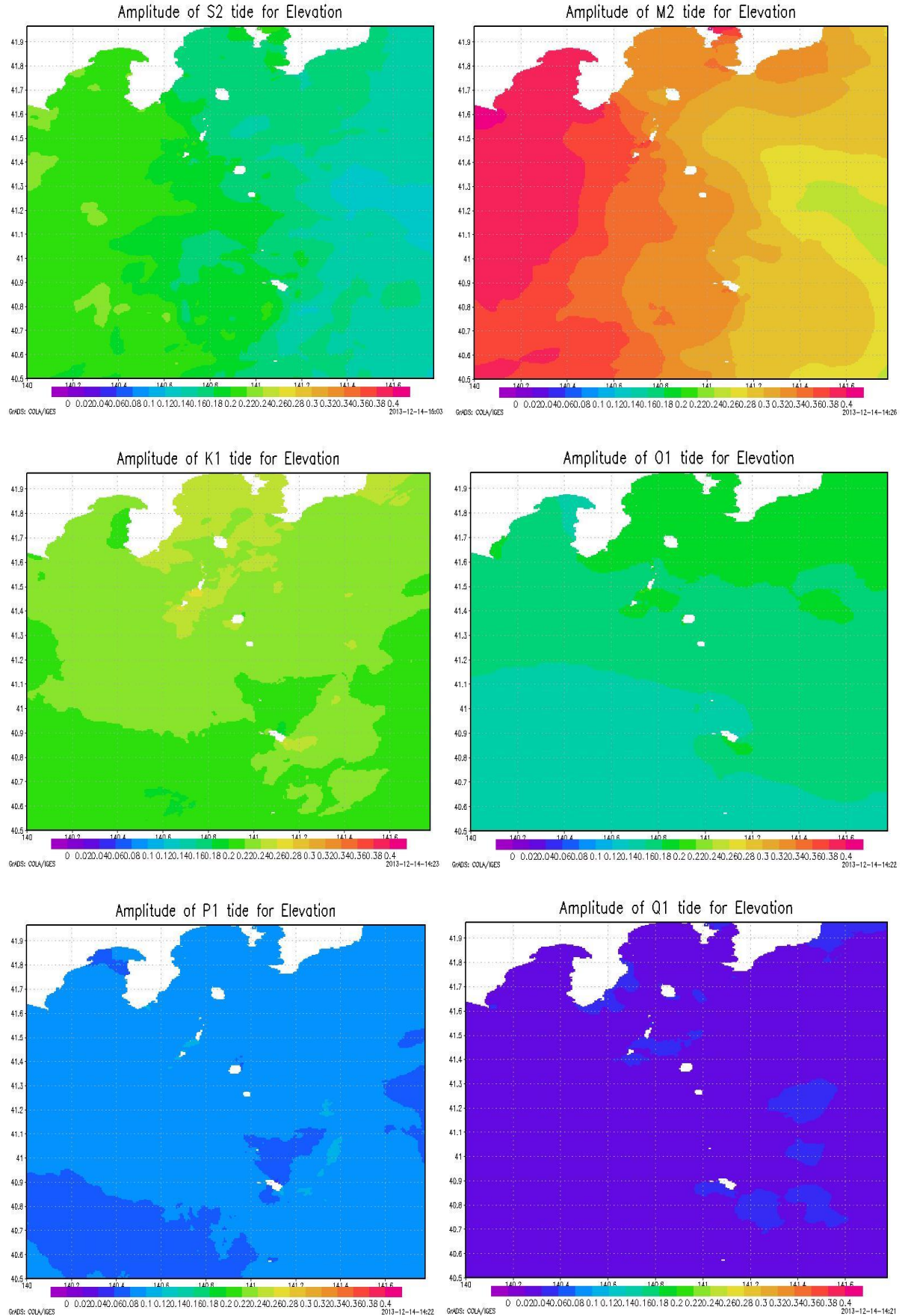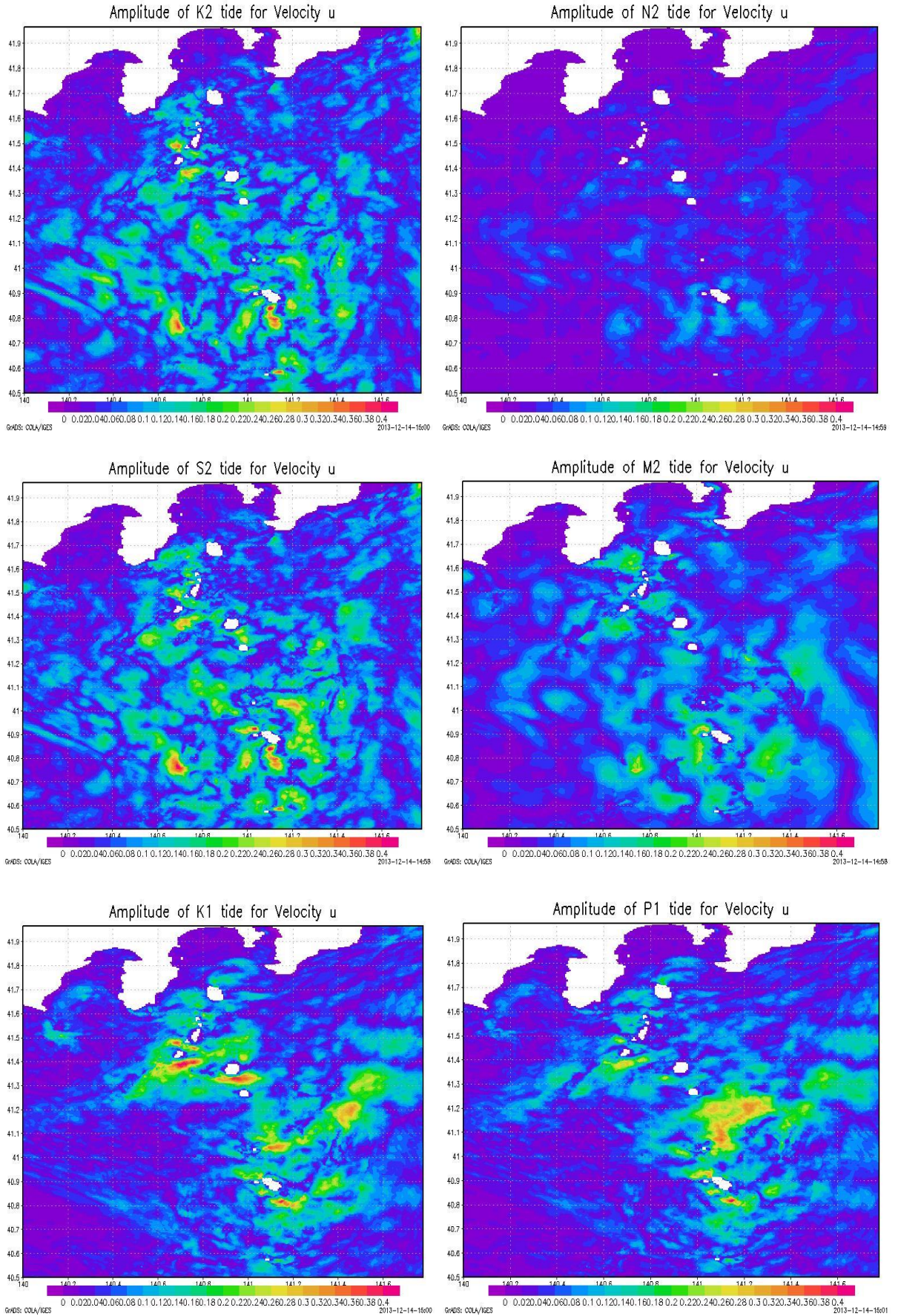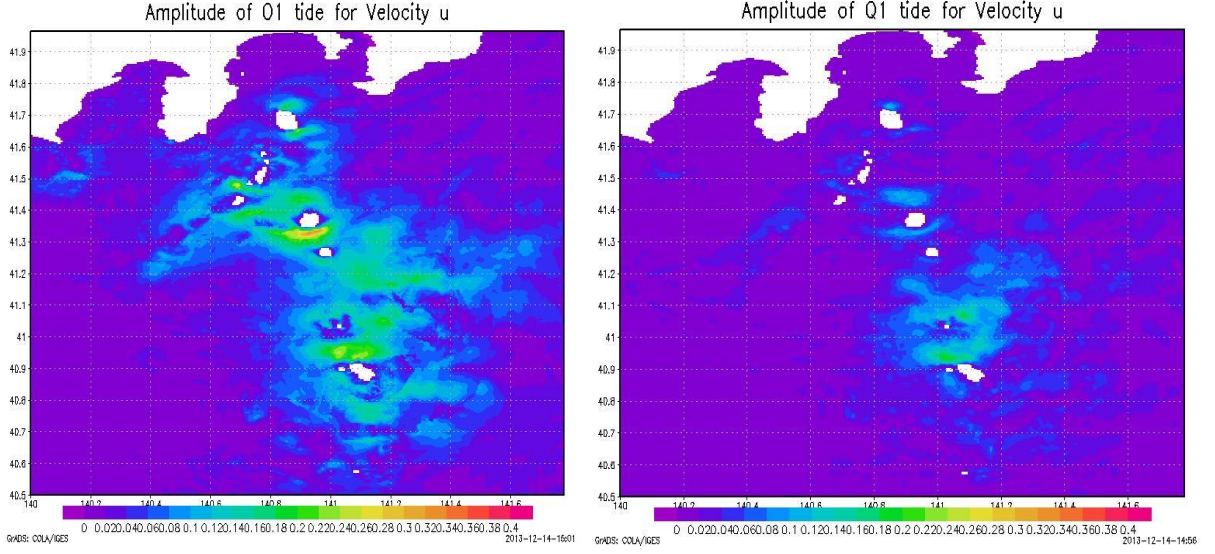In this section, we shall derive the dispersion relation of the ITWs based on the results given by Wunsch (1972) and Longuet-Higgins (1969). Neglecting the friction, dissipation and the advection terms, the governing equations for a flat-bottom ocean are:

$$u_t - fv = -\frac{1}{\rho_0}P'_x \tag{12}$$

$$v_t + fu = -\frac{1}{\rho_0}P'_y \tag{13}$$

$$w_t = -\frac{\rho'}{\rho_0}g - \frac{1}{\rho_0}P'_z \tag{14}$$

$$u_x + v_y + w_z = 0 \tag{15}$$

$$\rho'_t + w\rho_{0z} = 0 \tag{16}$$

Under the Boussinesq approximation, ρ_0 is the mean density field, taken to be constant expect in equation (16) and the primes represent the perturbation terms. For periodic phenomena in time i.e., $u, v, w, P \propto e^{-i\sigma t}$, the governing equations can be written as

$$-i\sigma u - fv = -\frac{1}{\rho_0}P'_x \tag{17}$$

$$-i\sigma v + fu = -\frac{1}{\rho_0}P'_y \tag{18}$$

$$-i\sigma w = -\frac{\rho'}{\rho_0}g - \frac{1}{\rho_0}P'_z \tag{19}$$

16

where σ is the frequency. From equation (17) and (18), we get

$$(\sigma^2 - f^2)v = -\frac{1}{\rho_0}\left(fP_x' + i\sigma P_y'\right) \tag{22}$$

$$(\sigma^2 - f^2)u = -\frac{1}{\rho_0}\left(i\sigma P_x' - fP_y'\right) \tag{23}$$

Therefore, taking the y and x partial derivative respectively,

$$(\sigma^2 - f^2)v_y = -\frac{1}{\rho_0}\left(fP_{xy}' + i\sigma P_{yy}'\right) \tag{24}$$

$$(\sigma^2 - f^2)u_x = -\frac{1}{\rho_0}\left(i\sigma P_{xx}' - fP_{yx}'\right) \tag{25}$$

Now, with a little algebra, we get from equations (19) and (21)

$$-i\sigma w - \frac{i}{\sigma}\frac{\rho_{0z}}{\rho_0}gw = -\frac{1}{\rho_0}P_z' \tag{26}$$

$$\therefore\ i\sigma^2 w - iN^2 w = \frac{\sigma}{\rho_0}P_z' \tag{27}$$

where, $N^2 = -g\rho_{0z}/\rho_0 = const.$ Therefore, taking the z partial derivative,

$$(\sigma^2 - N^2)w_z = -\frac{i\sigma}{\rho_0}P_{zz}' \tag{28}$$

Plugging in equations (24), (24) and (28) into equation (20) gives us the equation treated by Wunsch (1972)

$$P_{zz}' - \frac{N^2 - \sigma^2}{\sigma^2 - f^2}\left(P_{xx}' + P_{yy}'\right) = 0 \tag{29}$$

i.e.)

$$\frac{\partial^2 P'}{\partial z^2} + \frac{1}{\gamma^2}\nabla_H^2 P' = 0 \tag{30}$$

where Wunsch (1972) defined $\gamma^2 \equiv \frac{\sigma^2 - f^2}{N^2 - \sigma^2}$ and placed the sign between the two terms in

equation (30) minus, we have defined $\gamma^2 \equiv \frac{f^2 - \sigma^2}{N^2 - \sigma^2}$ since we will only focus on subinertial

frequencies i.e., $|\sigma| < f$. Separating, $P' = \varphi(z)\eta(r, \theta)$, we obtain

$$\frac{\gamma^2}{\varphi}\frac{\partial^2\varphi}{\partial z^2} = -\frac{1}{\eta}\nabla_H^2\eta = -\lambda^2$$

$$\therefore$$

$$\frac{\partial^2\varphi}{\partial z^2} + \frac{\lambda^2}{\gamma^2}\varphi = 0 \tag{31}$$

$$\nabla_H^2\eta - \lambda^2\eta = 0 \tag{32}$$

where λ^2 is the separation constant. If we now define

$$h_m \equiv \frac{f^2 - \sigma^2}{g\lambda^2} \qquad (33)$$

equation (32) becomes:

$$\nabla_H^2 \eta + \frac{\sigma^2 - f^2}{gh_m}\eta = 0 \qquad (34)$$

which corresponds to the equation treated by Longuet-Higgins (1969) when $|\sigma| < f$ for the barotropic case. The EQUIVALENT DEPTH h_m is determined from the vertical eigenvalue problem (16) subject to top and bottom boundary conditions.

In order to estimate h_m analytically, we shall make a rigid lid approximation and consider for N: $N = N_0 = const.$ For this case, from equation (16) we get:

$$\varphi(z) = A\, cos\left(\frac{\lambda}{\gamma}z\right) + B\, sin\left(\frac{\lambda}{\gamma}z\right). \qquad (35)$$

Due to the boundary conditions:

$$\frac{\partial \varphi}{\partial z} = 0 \qquad @\, z = 0, -H \qquad (36)$$

we obtain $\varphi(z) = A\, cos(m\pi z/H)$ and have

$$\lambda_m = \frac{m\pi}{H}\gamma$$

$$\qquad (37)$$

$$h_m = \frac{f^2 - \sigma^2}{g}\left(\frac{H}{m\pi}\right)^2\frac{1}{\gamma^2} \sim \frac{N^2 H^2}{g(m\pi)^2} \qquad (N^2 \gg \sigma^2)$$

where m is the vertical mode number. Applying this conclusion to the solution of equation (31) in a cylindrical coordinate given by Longuet-Higgins (1969) for a cylindrical island, we have

$$P'(r, \theta, z) = A\, cos(m\pi z/H)\, K_n(kr)e^{i(n\theta - \sigma t)} \qquad (38)$$

$$k^2 = \frac{f^2 - \sigma^2}{gh_m} \qquad (39)$$

for the solution of baroclinic ITW modes. $K_n(r)$ is the modified Bessel function of the second kind and it should be reminded that k is the radial wave number. We will now consider the boundary conditions at $r = a$, the edge of the island. Since the radial component of velocity vanishes, rewriting equation (1) ~ (5) in cylindrical coordinates and interpreting u, v as the radial and azimuthal horizontal velocity respectively, we obtain:

$$u = \frac{-g}{\sigma^2 - f^2}\left(i\sigma\frac{\partial P'}{\partial r} - \frac{f}{r}\frac{\partial P'}{\partial \theta}\right) = 0 \qquad @\, r = a \qquad (40)$$

Therefore, plugging in equation (38) into (40) gives us:

$$\frac{(ka)K_n'(ka)}{K_n(ka)} = \frac{nf}{\sigma} \qquad (41)$$

Using the recurrence relation: $K_n'(z) = \frac{n}{z}K_n(z) - K_{n+1}(z)$, equation (41) can be written as

$$\frac{(ka)K_{n+1}(ka)}{K_n(ka)} = n\left(1 - \frac{f}{\sigma}\right) \tag{42}$$

Now, from equation (39), we have:

$$\frac{\sigma}{f} = -\left(1 - \frac{(ka)^2}{\varepsilon}\right)^{\frac{1}{2}} \tag{43}$$

where

$$\varepsilon = \frac{f^2 a^2}{g h_m} = \left(\frac{m\pi a f}{NH}\right)^2 \ (\propto m^2) \tag{44}$$

Therefore, from equation (42) and (43), the boundary condition on $r = a$ reduces to:

$$F_n = -\frac{f}{\sigma} = G \tag{45}$$

where,

$$F_n = \frac{ka K_{n+1}(ka)}{n K_n(ka)} - 1, \qquad G = \left(1 - \frac{(ka)^2}{\varepsilon}\right)^{-\frac{1}{2}} \tag{46}$$

It comes down to the fact that equation (45), namely the dispersion relation, is all what we need to solve in order to derive the eigenfrequency σ of the ITWs.

3.2. Characteristics of the ITWs

Equation (25) indicates that σ is always negative, meaning that the ITWs progress clockwise in the northern hemisphere. In other words, the ITWs always progress with the island on their right hand side. Although this property seems very alike to Kelvin waves progressing along a straight coast line, ITWs should be considered differently from Kelvin waves. Firstly, ITWs have horizontal modes while Kelvin waves do not. Secondly, while the phase speed of Kelvin waves is:

$$c_{Kelvin} = \sqrt{g^* H} = NH \tag{47}$$

where g^* represents the reduced gravity, the azimuthal phase velocity of the ITWs is derived from equation (45), the dispersion relation. When ka is large compared to n, the value of K_{n+1}/K_n converges to unity (Fig. 13) so Longuet-Higgins (1969) has shown that F_n can be reduced asymptotically as:

$$F_n \sim \frac{ka}{n} \tag{48}$$

Since $ka \gg n$, equation (45) tells us that G should also have a large value and gives us:

$$ka \sim \sqrt{\varepsilon}$$

$$\therefore \ -\frac{f}{\sigma} = F_n \sim \frac{\sqrt{\varepsilon}}{n} \tag{49}$$

Longuet-Higgins (1969) only considered the phase speed for barotropic ITWs. For baroclinic

ITWs, equation (49) can be written as:

$$-\frac{f}{\sigma} = \frac{af}{n\sqrt{gh_m}} \tag{50}$$

by substituting equation (44) into equation (49). Hence, the phase speed at the boundary of the island is

$$\therefore \ c_{ITW} = n\sqrt{gh_m} = \frac{n}{m\pi}NH \tag{51}$$

Equation (47) and (51), tell us that for $n = 1, \ 2$ and 3, ITWs will always have smaller phase speeds than Kelvin waves. L-H has given the solution of (45) in terms of $-\sigma/f$ as a function of ε and it will be reproduced in Fig. 14.
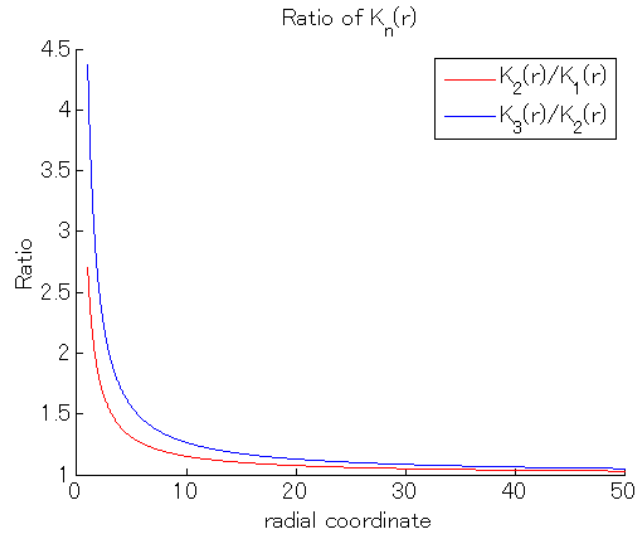

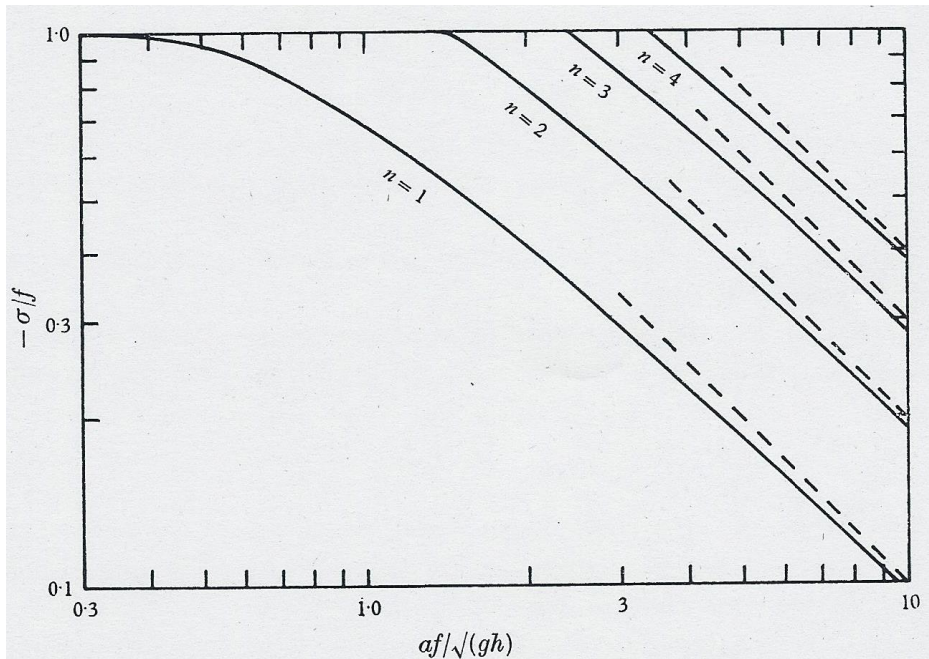Figure 13. Value of $K_{n+1}(r)/K_n(r)$.

20

Figure 14. Solution of (27) in terms of $-\sigma/f$ as a function of $\sqrt{\varepsilon}$. Taken from Longuet-Higgins (1969).

3.3. Application to the observations around the Miyake Island

The solution for the fundamental mode $(n,m) = (1,1)$ is:

$$P'(r,\theta,z) = A\cos(\pi z/H)\,K_1(kr)e^{i(\theta-\sigma t)} \tag{52}$$

$$h_1 = \frac{N^2 H^2}{g\pi^2}\,, \qquad k^2 = \frac{\pi^2}{N^2 H^2}(f^2 - \sigma^2)\,, \qquad \varepsilon = \left(\frac{\pi a f}{NH}\right)^2 \tag{53}$$

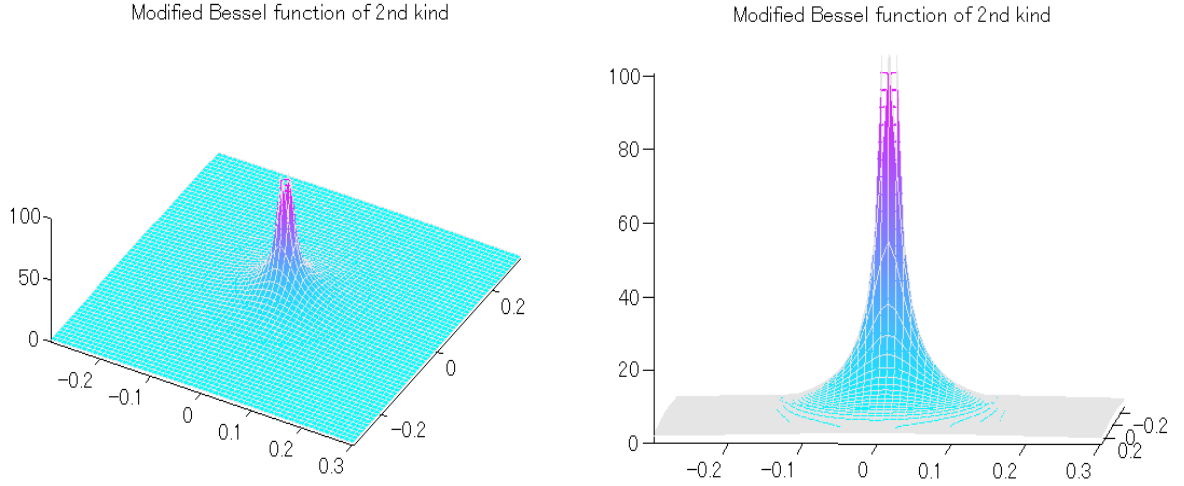We will show the configuration of $K_1(r)$ in Fig. 15.

Figure 15. Diagram of $K_1(r)$. We see that the amplitude decays rapidly as r increases.

Equation (44) implies that we need the density profile to obtain the eigenperiods of the ITWs so we will estimate the density profile close to that around Miyake Island in March, 2011 from the equations:

$$\rho(S,\Theta,P) = \rho_\theta(S,\Theta) + \rho_P(S,\Theta,P) \tag{54}$$

where

$$\begin{aligned}
\rho_\theta = {} & 999.842594 + 6.793952 \times 10^{-2}\Theta - 9.095290 \times 10^{-3}\Theta^2 + 1.001685 \times 10^{-4}\Theta^3 \\
& - 1.120083 \times 10^{-6}\Theta^4 + 6.536332 \times 10^{-9}\Theta^5 \\
& + (0.824493 - 4.0899 \times 10^{-3}\Theta + 7.6438 \times 10^{-5}\Theta^2 - 8.2467 \times 10^{-7}\Theta^3 \\
& + 5.3875 \times 10^{-9}\Theta^4)S \\
& + (-5.72466 \times 10^{-3} + 1.0227 \times 10^{-4}\Theta - 1.6546 \times 10^{-6}\Theta^2)S^{3/2} \\
& + 4.8314 \times 10^{-4}S^2
\end{aligned} \tag{55}$$

$$\rho_P = 1.0 \times 10^4 P c^{-2}(1.0 - 0.20Pc^{-2}) \tag{56}$$

$$c = 1449 + 0.00821P + 4.55\Theta - 0.045\Theta^2 + 1.34(S - 35.0) \tag{57}$$

which are given by Mellor[9] (1991). Θ is potential temperature in °C; S is salinity in psu and
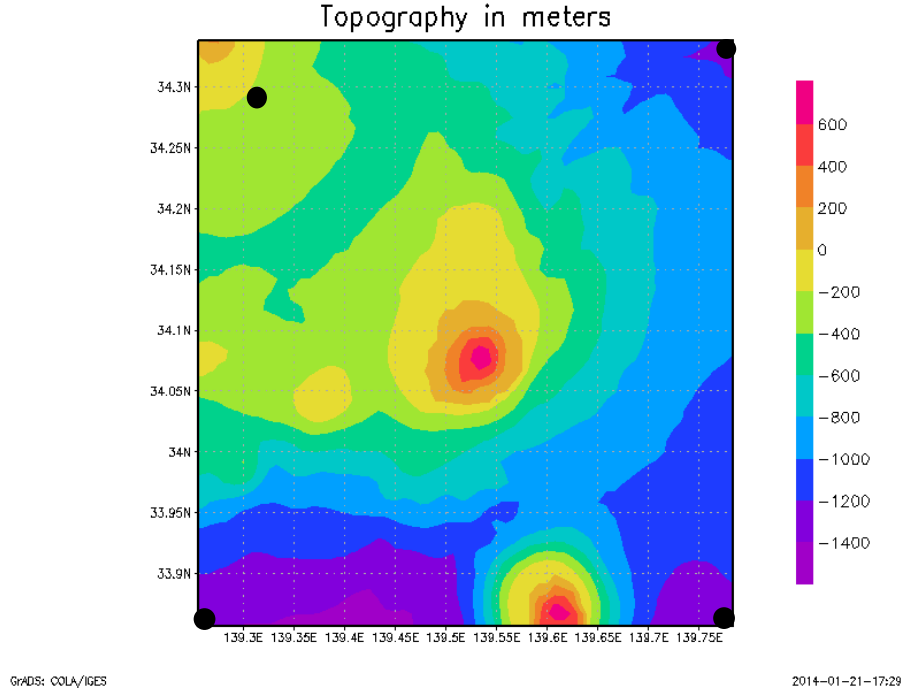
Figure 16. Topography with Miyake Island lying in the center. The black dots indicate the four points where the profiles of potential temperature and salinity were taken. The topographic data used in the reanalysis data was not available so the topography represented in the figure and used in the reanalysis data are not identical.
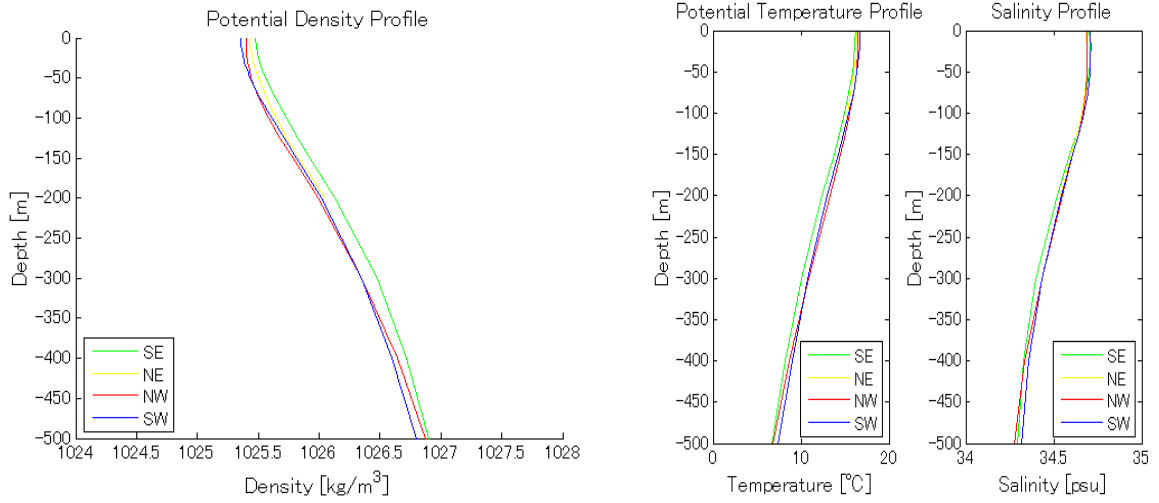
Figure 17. Monthly averaged profiles of the potential density (ρ_θ), potential temperature (θ) and salinity (S) taken at the four points in Fig. 16 in March, 2011. SE: southeast, NE: northeast, NW: northwest, SW: southwest.

When the temperature data is provided as in-situ temperature, equation (54) requires us to convert the in-situ temperature into potential temperature (Appendix A). Since the temperature results of sbPOM are provided as potential temperature, we can simply obtain the density profile from equations (54) ~ (57).

Table 1 indicates the properties of density taken from the four points shown in Fig. 16 against depth. The reason why the variance is truncated at 200 m depth is because the northeast

corner only has data until that depth while the rest have data until 1000 m depth. We see that the percentage of error (ratio of standard deviation and 30 day average) is less than 1% for each depth so we will use the spatial averaged potential density profile, calculated from the four points in deriving the Brunt-Vaisala frequency.

Table 1. Properties of the monthly averaged density (ρ) profile of the four points shown in Fig. 14 in March, 2011

Depth(m)	Variance	Standard Deviation (kg/m^3)	30 day Average(kg/m^3)	Percentage of Error
0	0.0026	0.0510	1025.4	0.50%
−10	0.0028	0.0529	1025.5	0.52%
−20	0.0029	0.0539	1025.5	0.53%
−30	0.003	0.0548	1025.6	0.53%
−40	0.0033	0.0574	1025.6	0.56%
−50	0.0035	0.0592	1025.7	0.58%
−75	0.0038	0.0616	1025.9	0.60%
−100	0.0039	0.0624	1026.1	0.61%
−125	0.0039	0.0624	1026.3	0.61%
−150	0.0038	0.0616	1026.5	0.60%
−200	0.004	0.0632	1026.9	0.62%
−300	NaN	NaN	1027.7	NaN
−400	NaN	NaN	1028.5	NaN
−500	NaN	NaN	1029.1	NaN
−1000	NaN	NaN	1032	NaN

To derive the gradient of the potential density, we will make a linear approximation of the profile of the potential density by dividing the difference of the spatially averaged potential density $\bar{\rho}_\theta$, derived from the four points in Fig. 16, between 0 m depth and 500 m depth with depth, i.e.)

$$\rho_{0z} \sim \frac{\bar{\rho}_\theta|_{z=H} - \bar{\rho}_\theta|_{z=0}}{H}$$

$$= \frac{1026.9 - 1025.4}{500} = 0.0029 \ kg/m^4 \tag{58}$$

and

$$\rho_0 = \frac{1}{H} \sum_{z=0}^{z=H} \bar{\rho}_\theta \sim 1025.8 \ kg/m^3 \tag{59}$$

From the values above, we get

$$N^2 \sim 2.773 \times 10^{-5} \ sec^{-2}$$

$$\therefore N \sim 5.3 \times 10^{-3} \ r/sec \ (= 3.02 \ cph) \tag{60}$$

Using this value and from equation (6), (7) and (20), we have

$$u, v \propto e^{i(n\theta - \sigma t)} \tag{61}$$

so when θ is taken from 0 rad. to 2π rad., for $n = 1$, the horizontal velocity will have 2 nodes and for $n = 2$, the horizontal velocity will have 4 nodes as shown in Fig. 18.
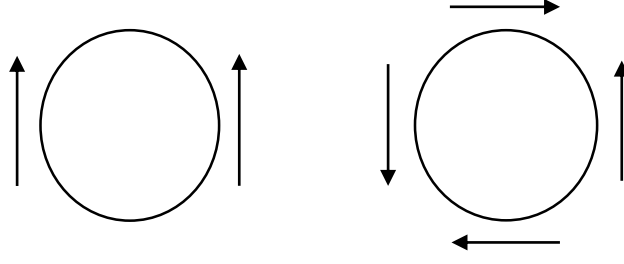
Figure 18. Pattern diagram around a circular island of the distribution of azimuthal horizontal velocity v. The magnitude of the arrows is not held to scale. The left and right diagram represent the pattern for $n = 1$ and $n = 2$ respectively. For $n = 1$, there is one converging and diverging point. As for $n = 2$, there are two converging and diverging points respectively.

Comparing the patterns of the velocity vectors shown in the 1st, 2nd and 3rd CEOF mode (Fig. 7) with the patterns shown in Fig. 17, the 1st and 2nd CEOF mode seem to correspond to the horizontal mode number of the ITWs $n = 1$ and the 3rd CEOF mode to $n = 2$. We will, therefore, derive the eigenperiod for $n = 1, 2$; the horizontal mode and $m = 1, 2$; the vertical mode number since it is unlikely that higher modes would be excited due to higher damping. From equation (26) and (27), when $a = 10$ km, $H = 500$ m, $f = 8.147 \times 10^{-5}$ r/sec ($= 4\pi \sin(34°4')/24 = 21.42$ hours), and $(n, m) = (1, 1)$, we have:

$$\varepsilon = \left(\frac{\pi a f}{NH}\right)^2 = 0.9328 \qquad \therefore \varepsilon^{\frac{1}{2}} = 0.9658$$

$$k = 6.920 \times 10^{-5}, \qquad \sigma \sim -0.6976f \ (= 30.71 \text{ hours})$$

and the phase speed at the boundary is: $\qquad\qquad\qquad\qquad\qquad$ (62)

$$c_{(1,1)} = a\sigma \sim 0.568 \text{ m/s}$$

For $(n, m) = (2, 1)$, equation (27) does not have any solutions so when $(n, m) = (2,2)$:

$$\varepsilon = \left(\frac{2\pi a f}{NH}\right)^2 = 3.731 \qquad \therefore \varepsilon^{\frac{1}{2}} = 1.932$$

$$k = 1.102 \times 10^{-4}, \qquad \sigma \sim -0.8213f \ (= 26.08 \text{ hours})$$

and $\qquad\qquad\qquad\qquad\qquad\qquad\qquad\qquad\qquad\qquad\qquad\qquad$ (63)

$$c_{(2,2)} = a\sigma \sim 0.669 \text{ m/s}$$

The phase speeds shown in Fig. 11 were certainly not taken at the boundary and the paths shown in Fig. 2 were not circular. Suppose the radius is taken as 15 km and $c_{(2,2)} = r\sigma \sim 1$ m/s. Considering the errors of the path length, the phase speeds derived from cross spectrum on the east side of Miyake Island seem to agree quite well with the theoretical phase speed when the radius is taken as 15 km. Another point worth noting is that the eigenperiod of $(n, m) = (2, 2)$ lies remarkably close to the periods of K1, P1, O1 and Q1 tidal components. This strongly suggests the possibility of tidal forced ITWs being excited around Miyake Island.

When a symmetrical shoaling region exists instead of a flat-bottom ocean, assuming a solution: $u, v, w, P' \propto \psi(r, z)e^{i(n\theta - \sigma t)}$, the boundary condition at the shoaling can be derived from:

$$-i\sigma u - fv = -\frac{1}{\rho_0}P_r' \tag{64}$$

$$-i\sigma v + fu = -\frac{1}{\rho_0}\frac{in}{r}P' \tag{65}$$

$$(\sigma^2 - N^2)w = -\frac{i\sigma}{\rho_0}P_z' \tag{66}$$

$$w(-h) = \frac{D(-h)}{Dt} = -uh_r \tag{67}$$

as

$$\frac{h_r}{f^2 - \sigma^2}\left(n\frac{f}{r}P' - \sigma P_r'\right) = \frac{\sigma}{N^2}P_z' \qquad @ \; z = -h(r) \tag{68}$$

the equation treated by Hogg (1980). When $\sigma \ll f$ equation (68) reduces to

$$\frac{\sigma}{N^2}P_z' = \frac{h_r}{f}\frac{n}{r}P'$$

$$\therefore \; \frac{\sigma}{N^2}\psi_z = \frac{n}{f}\frac{h_r}{r}\psi \qquad @ \; z = -h(r) \tag{69}$$

Therefore, the solution of equation (31) when $N \gg f \gg \sigma$: $\varphi(z) = \cos\left(\frac{\lambda}{\gamma}z\right) \sim \cos\left(\lambda\frac{N}{f}z\right)$

needs to satisfy equation (69). When r is considered as a constant, it is possible to separate ψ

so, plugging the equation above into equation (69), gives us:

$$-\sin\left(\lambda\frac{N}{f}(-h)\right)\lambda\frac{N}{f} = \frac{N^2}{\sigma}\frac{nh_r}{rf}\cos\left(\lambda\frac{N}{f}(-h)\right)$$

$$\therefore \; \delta\tan(\delta) = \frac{N^2}{\sigma}\frac{nh_r}{rf}h \; (\gg 1) \tag{70}$$

where $\delta = \lambda\frac{N}{f}(-h)$ (< 0). Since the value on the right hand side of equation (70) is much

larger than unity, the solution for this can be given as:

$$\lambda_m^s = \lambda \sim \left(\frac{2m-1}{2}\right)\frac{\pi f}{N}\frac{1}{h} \tag{71}$$

which is the inverse of the decay scale when a shoaling region exists. From equation (71), when
$m = 1$ we have

$$\varepsilon^s = (a\lambda_m^s)^2 = \left(\frac{1}{2}\frac{\pi a f}{N}\frac{1}{h}\right)^2 \tag{72}$$

Comparing equation (53) and (72):

$$\varepsilon^s = \left(\frac{H}{2h}\right)^2\varepsilon \tag{73}$$

Therefore when the equivalent depth h is larger than half of the depth H, we will have smaller
"ε"s, resulting in shorter fundamental eigenperiods than 30 hours.

4. Numerical Experiment

Since the governing equations treated in the ITW theory are linearized, theory does not provide information about the effects of non-linear terms, change in topography, and bottom friction. The aim of our numerical simulation was to clarify whether a resonant system really existed, observe the spatial patterns of the ITWs, and understand the effects of non-linear terms. In this study, we shall show the effects of bottom friction on the eigenperiods. The basic equations for our calculation in sigma coordinates (Fig. 19) are:

$$\frac{\partial UD}{\partial x} + \frac{\partial VD}{\partial y} + \frac{\partial w}{\partial \sigma} + \frac{\partial \eta}{\partial t} = 0 \tag{74}$$

$$\frac{\partial UD}{\partial t} + \frac{\partial U^2 D}{\partial x} + \frac{\partial UVD}{\partial y} + \frac{\partial Uw}{\partial \sigma} - fVD + gD\frac{\partial \eta}{\partial x} + \frac{gD^2}{\rho_0}\int_\sigma^0 \left[\frac{\partial \rho'}{\partial x} - \frac{\sigma'}{D}\frac{\partial D}{\partial x}\frac{\partial \rho'}{\partial \sigma'}\right] d\sigma'$$

$$= \frac{\partial}{\partial \sigma}\left[\frac{K_M}{D}\frac{\partial U}{\partial \sigma}\right] + F_x \tag{75}$$

$$\frac{\partial VD}{\partial t} + \frac{\partial UVD}{\partial x} + \frac{\partial V^2 D}{\partial y} + \frac{\partial Vw}{\partial \sigma} + fUD + gD\frac{\partial \eta}{\partial y} + \frac{gD^2}{\rho_0}\int_\sigma^0 \left[\frac{\partial \rho'}{\partial y} - \frac{\sigma'}{D}\frac{\partial D}{\partial y}\frac{\partial \rho'}{\partial \sigma'}\right] d\sigma'$$

$$= \frac{\partial}{\partial \sigma}\left[\frac{K_M}{D}\frac{\partial V}{\partial \sigma}\right] + F_y \tag{76}$$

$$\frac{\partial q^2 D}{\partial t} + \frac{\partial U q^2 D}{\partial x} + \frac{\partial V q^2 D}{\partial y} + \frac{\partial w q^2}{\partial \sigma}$$

$$= \frac{\partial}{\partial \sigma}\left[\frac{K_q}{D}\frac{\partial q^2}{\partial \sigma}\right] + \frac{2K_M}{D}\left[\left(\frac{\partial U}{\partial \sigma}\right)^2 + \left(\frac{\partial V}{\partial \sigma}\right)^2\right] + \frac{2g}{\rho_0}K_H\frac{\partial \rho}{\partial \sigma} - \frac{2Dq^3}{B_1} + F_q \tag{77}$$

$$\frac{\partial q^2 lD}{\partial t} + \frac{\partial U q^2 lD}{\partial x} + \frac{\partial V q^2 lD}{\partial y} + \frac{\partial w q^2 l}{\partial \sigma}$$

$$= \frac{\partial}{\partial \sigma}\left[\frac{K_q}{D}\frac{\partial q^2 l}{\partial \sigma}\right] + E_1 l\left(\frac{K_M}{D}\left[\left(\frac{\partial U}{\partial \sigma}\right)^2 + \left(\frac{\partial V}{\partial \sigma}\right)^2\right] + E_3\frac{g}{\rho_0}K_H\frac{\partial \rho}{\partial \sigma}\right) - \frac{Dq^3}{B_1}\widetilde{W}$$

$$- F_l \tag{78}$$

where

$$F_x = \frac{\partial}{\partial x}\left(2HA_M\frac{\partial U}{\partial x}\right) + \frac{\partial}{\partial y}\left(2HA_M\left(\frac{\partial U}{\partial y} + \frac{\partial V}{\partial x}\right)\right)$$

$$F_y = \frac{\partial}{\partial y}\left(2HA_M\frac{\partial V}{\partial y}\right) + \frac{\partial}{\partial x}\left(2HA_M\left(\frac{\partial U}{\partial y} + \frac{\partial V}{\partial x}\right)\right)$$

$$F_\varphi = \frac{\partial}{\partial x}\left(HA_H\frac{\partial \varphi}{\partial x}\right) + \frac{\partial}{\partial y}\left(HA_H\frac{\partial \varphi}{\partial y}\right)$$

and φ represents q^2 or $q^2 l$. The conversion from Cartesian coordinates to sigma coordinates will be shown briefly in Appendix C. q^2 represents twice the turbulence kinetic energy; l is the turbulence length scale and w is the transformed vertical velocity which represents the

velocity component perpendicular to the sigma surfaces. Further explanation about the equations can be referred to the user's guide of POM[10] (2004).
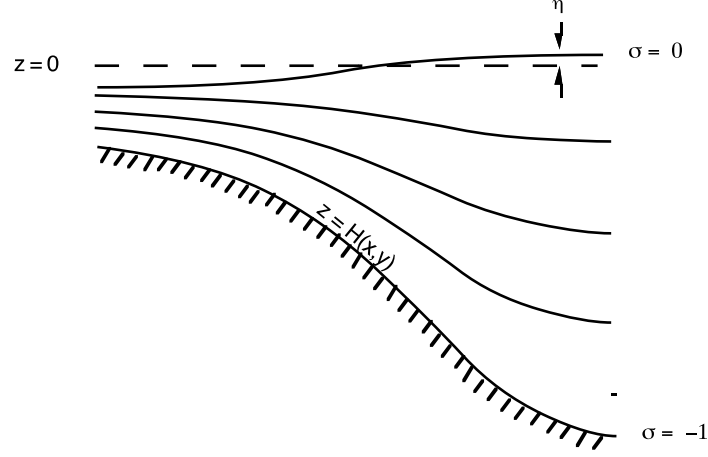

Figure 19. The sigma coordinate system. Sigma coordinate is placed so as it follows the bottom topography. Taken from the user's guide of POM (2004).
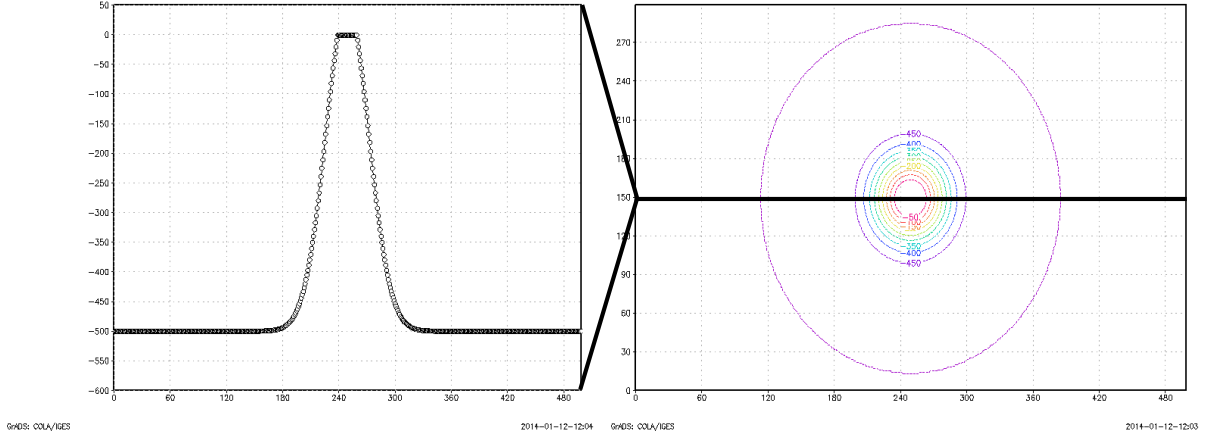

Figure 20. Diagram of cross section and contour map showing the topography used in the numerical experiment. The horizontal scale is in kilometers and the vertical scale is in meters.

The horizontal resolution was 1 km (500×300 grids) and the vertical resolution was 16 levels in a sigma coordinate with uniform depth of 500 m. The island was placed in the center of the domain with radius of 10 km and a sloping with a configuration of a bell curve:

$$h = H\left(1 - dh \exp\left[-\frac{r^2}{R^2}\right]\right) \tag{79}$$

where $H = 500$ m, $dh = 1.1$, $R = 32.39$ km, which was truncated at $h = 0$ m (Fig. 20). h represents the depth of the shoaling region and joins H where the slope ends. The boundary conditions were radiation on all sides except for the west boundary where we clamped an elevation condition of arbitrary frequencies in order to produce a quasi-tidal forced field. For each frequency, the simulation was run for 40 days. The radiation equation for the external mode was:

27

$$H\bar{U} \pm \sqrt{gH}\eta = 0 \tag{80}$$

where $\bar{U}$ is the vertically averaged horizontal velocity.

For the internal mode:

$$\frac{\partial U}{\partial t} \pm c\frac{\partial U}{\partial x} = 0 \tag{81}$$

The finite difference expression of the equation above for the east version can be given as:

$$U_{im}^{n+1} = \alpha U_{im-1}^{n} + (1-\alpha)U_{im}^{n} ; \quad \alpha \equiv c\Delta t/\Delta x \tag{82}$$

where we have set $\alpha = 1/9$. This may seem like a crude approximation but Mellor (2004) has given that this performs fairly well as long as $0 < \alpha \leq 1$. The elevation condition on the east boundary was set as:

$$\eta = A\sin(\sigma_F t) \tag{83}$$

where σ_F was the forcing frequency and the amplitude A was set to 10 cm (e.g. Ohwaki el al. (1994)). Applying the f-plane approximation, the inertial period was set to 21.42 hours, equivalent to the inertial period around Miyake Island.

To simplify the numerics, we held the temperature and salinity fixed. When temperature and salinity are held fixed, the perturbation term ρ' in equations (1) ~ (5) cannot be generated. With the addition that $\rho_{0z} \neq 0$, equation (5) tells us that there is no vertical velocity inside of the fluid i.e., $w = 0$. Therefore, equations (1) ~ (5) reduce to:

$$u_t - fv = -\frac{1}{\rho_0}P_x \tag{1}$$

$$v_t + fu = -\frac{1}{\rho_0}P_y \tag{2}$$

$$0 = -\rho_0 g - P_z \tag{3}$$

$$u_x + v_y + w_z = 0 \tag{4}$$

and results in:

$$u_t - fv = -\frac{1}{\rho_0}\eta_x \tag{1'}$$

$$v_t + fu = -\frac{1}{\rho_0}\eta_y \tag{2'}$$

$$P = \rho_0 g(\eta - z) \tag{3'}$$

$$\eta_t + (u_x + v_y)H = 0 \tag{4'}$$

Equation (1') ~ (4') are the governing equations of barotropic conditions so the effects of density stratification are expected to be small. Verification of this assumption will be shown in Appendix A. We see from Fig. 21 that the north-south component of horizontal velocity turns out to be barotropic as expected.
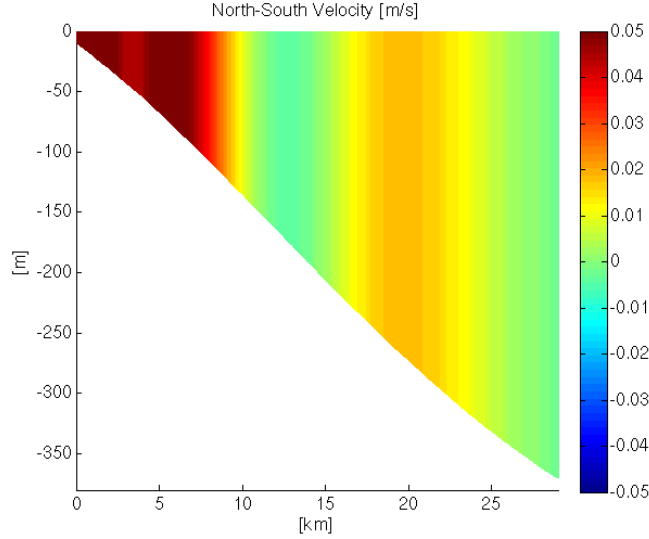
Figure 21. A snapshot of north-south component of horizontal velocity at a certain time when there was no bottom friction.

4.1. Effects of bottom friction

Since we are considering a barotropic condition, when a resonance occurs an amplification in sea-surface elevation $(= \eta)$ should appear. We, therefore, took the ratio of the sea-surface elevation with and without an island at the same point, viz.

$$\frac{\eta_{with\ island}}{\eta_{without\ island}}$$

in determining the resonant period.

The response functions for both cases, with non-zero bottom friction and without bottom friction, will be shown in Fig. 22. When a non-zero bottom friction exists, the eigenperiod is expected to become longer. This can be easily understood in analogy to a forced oscillation of a spring with damping [Appendix C]. It seems that bottom friction does affect the eigenperiods considering that the resonant period shifted from 25.5 hours when there was no bottom friction to 27 hours when there was non-zero bottom friction. This suggests that bottom friction may be a non-negligible factor in determining the eigenperiods.

For the case without bottom friction, we will show the Hopf-Mellor diagram of vertically averaged horizontal velocity when the forcing period was 25.5 hours as a representative example in Fig. 23. The diagonal patterns show the existence of waves progressing around the island as in Fig. 3 and Fig. 4. Fig. 24 shows the 1st and 2nd mode of CEOF analysis conducted for horizontal velocity at depth 0 m when the forcing period was 25.5 hours. In Fig. 25 are shown the principle components corresponding to each CEOF mode respectively and we see that the pattern shown as the 1st CEOF mode, which is expected to represent the 1st ITW horizontal mode, rotates around the island with a period equivalent to the forcing period.

29

For the case when a non-zero bottom friction existed, we will show the result of CEOF analysis of horizontal velocity at depth 0 m when the forcing period was 27 hours in Fig. 26 as a representative example. The principle component (Fig. 27) tells us that the pattern shown as the 1st CEOF mode, which is expected to represent the 1st ITW horizontal mode, rotates around the island with a period equivalent to the forcing period even when bottom friction exists.
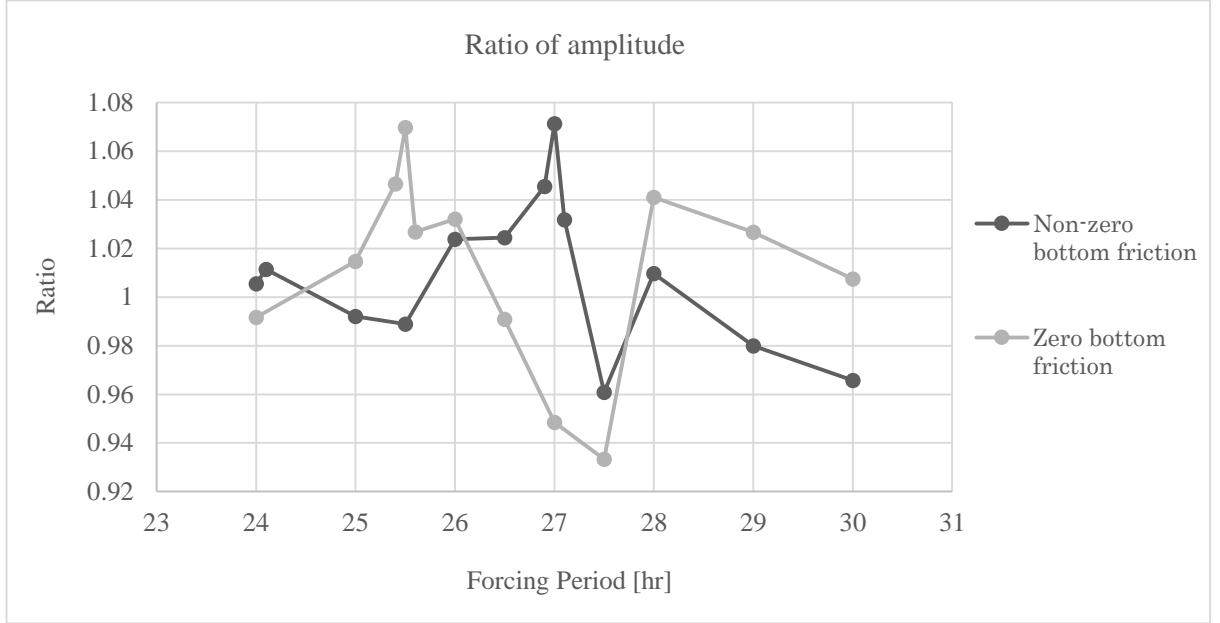

Figure 22. Ratio of elevation amplitude between calculation with island and without island when there was no bottom friction.
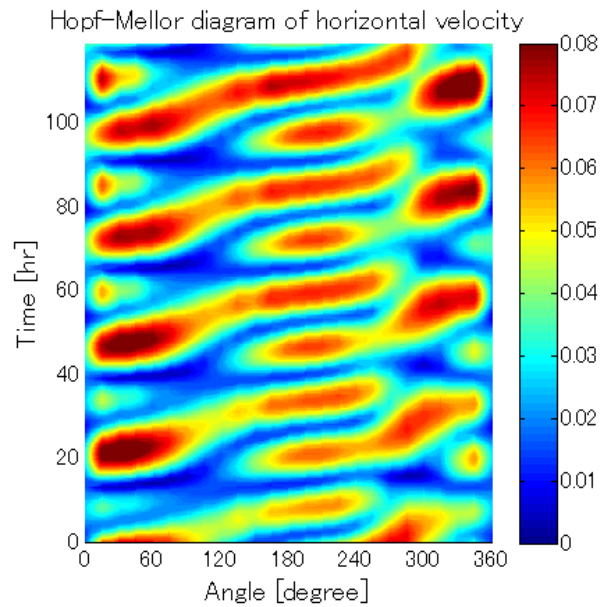
Figure 23. Hopf-Mellor diagram of the magnitude of vertically averaged horizontal velocity. The color bar represents m/s.
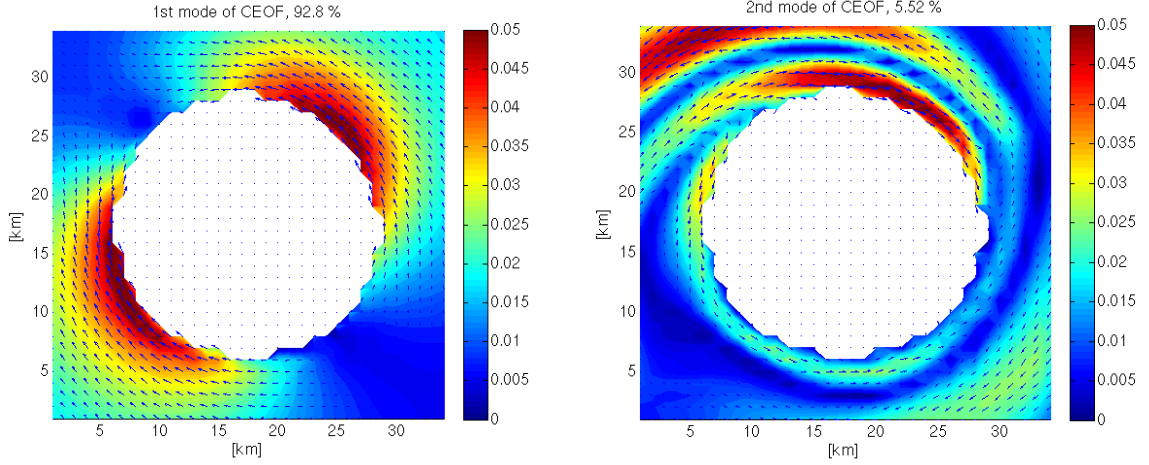

Figure 24. The 1st and 2nd CEOF mode when there was no bottom friction. The 1st CEOF mode is expected to represent the 1st ITW horizontal mode. The scale of the velocity vectors is preserved.
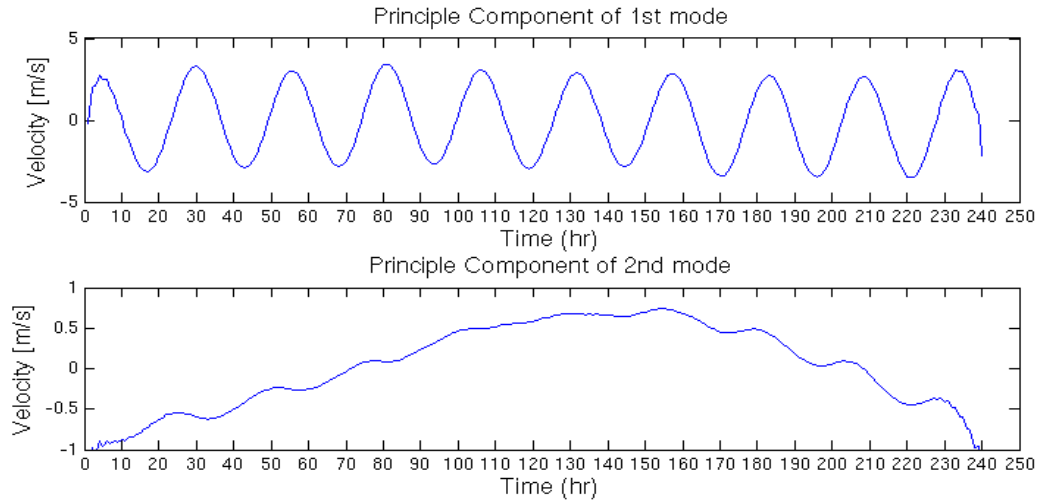

Figure 25. The principle component of the CEOF 1st and 2nd mode in Fig. 24.
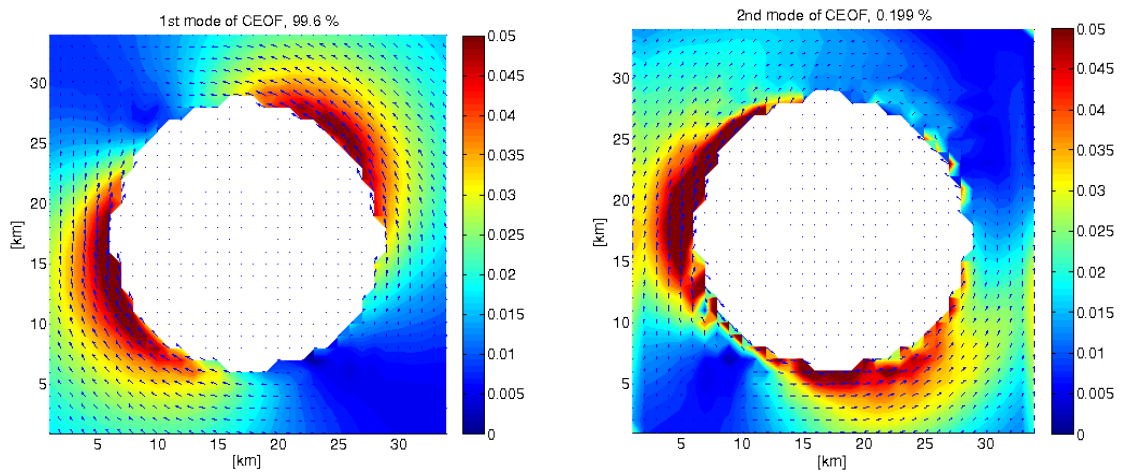
Figure 26. The 1st and 2nd CEOF mode when there was non-zero bottom friction. The 1st CEOF mode is expected to represent the 1st ITW horizontal mode. The scale of the velocity vectors is preserved.
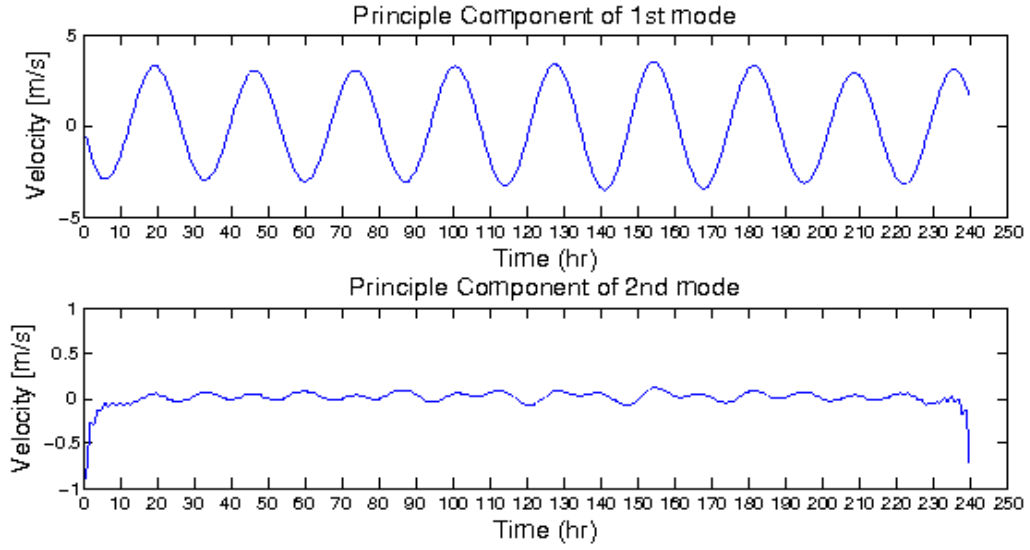

Figure 27. The principle component of the CEOF 1st and 2nd mode in Fig. 26.

5. Summary & Discussion

The Hopf-Mellor diagrams, show positive evidence for the existence of currents circulating around the Miyake Island and the Hachijo Island and the Fourier analysis and cross spectral analysis indicate that the circulating currents have periods close to the K1, P1, O1 and Q1 tidal component.

We have attempted to explain the circulating currents by assuming that they were tidal forced ITWs. The ITW theory indeed supports the analyzed results by providing an explanation for the horizontal modal structures found by EOF/CEOF analysis and suggesting the possibility of resonant modes lying in the vicinity of the astronomical tidal periods. Furthermore, it seems that the non-dimensional parameter $\sqrt{\varepsilon} = a/(\sqrt{gh_m}/f)$; the ratio of the radius of the island and the Rossby deformation scale, would become smaller and, hence, the eigenperiods of the ITWs will become shorter when a shoaling region exists. Considering that the period of the fundamental mode was 30 hours, and that this would become closer to the K1, P1, O1 and Q1 tidal component when a shoaling region exists, it is tempting to conclude that the circulating currents observed around Miyake Island and Hachijo Island are ITWs excited by internal tides.

The numerical results support this conclusion. In other words, when elevation conditions representing tidal forcing were prescribed at the western boundary, a resonance occured when the period of the forcing was equivalent or close to the eigenperiod of the ITWs. Although the topography had an ideal configuration, the sharp peaks in Fig. 21 and Fig. 25 suggest that the range eigenperiods of the ITWs are very narrow and, hence, it is likely that, by coincidence, the

From equation (26), it is obvious that the eigenperiods are very sensitive to the values of sea depth, radius of the island, and Brunt-Vaisala frequency. Smaller sea-floor depth, Brunt-Vaisala frequency, and larger radius result in larger values of "ε"s, hence, as we can see from Fig. 12, longer eigenperiods. The other way around is equivalently true. By adjusting the parameters, therefore, it is possible to make the theory a better fit but this would not gain us much.

While we have concluded that the ITWs were excited by tides, our discussion does not exclude the possibility of other forcings such as wind. As mentioned by Brink (1999), however, the effectiveness of wind forcing decreases as the radius of the island decreases so it seems unlikely that small islands such as the Miyake Island could excite wind-forced ITWs. This conclusion that the circulating currents were not wind driven is also supported by the fact that the circulating currents were internal and observed in the reanalysis data for almost throughout a month during December and March. Although winter and spring are windy seasons, the probability is low for winds, which have large fluctuations, to excite ITWs constantly throughout a whole month.

Explanation of the seasonal variability, namely that the circulating currents were not observed in summer could be ascribed to the location of the Kuroshio path. While the Kuroshio passed the southern quarter of the Izu-Islands from winter 2011 until spring 2012, the islands were right in the path of the Kuroshio during the summer, possibly causing the signals of the ITWs to drown out. It would be interesting to analyze data in summer when the Kuroshio is far away from the Izu-Islands.

Some caveats are required. Although the Brunt-Vaisala frequency was taken as a constant in theory, it was dependent on the vertical coordinate in reality. However, the deviance from the assumption that we made, namely a linear approximation for the potential density profile, was expected to be small enough so that the theory could be applicable in explaining the ITWs around the Miyake Island. Secondly, temperature and salinity are certainly not fixed and the topography is not symmetrical in the real ocean, unlike in our numerical experiment. This does not undermine the fact, however, that the numerical results demonstrate the possibility of tidal forcing ITWs being excited around islands.

Further evidence for tidal forced ITWs could perhaps be referred to the discussion in Kowalik and Proshutinsky[16] (1995) and Kowalik and Stabeno[15] (1999), where the existence of semidiurnal trapping of external modes caused by the M2 tide around the islands is suggested. However, the inertial period is around 12.45 hours (Longitude: 19°01′E, Latitude: 74°31′N) in the region around the Bear Island and 14.31 hours (Longitude: 170°W, Latitude: 57°N) in the region of the Pribilof Islands, which are both slightly longer than the M2 period (12.42 hours).

Since complete trapping is not possible when the periods of the ITWs are shorter than the inertial period, the dipole structures of sea-surface elevation propagating clockwise around the islands, mentioned in both papers, are possibly a result of virtual trapping, as given in L-H. Besides shelf waves, ITWs around islands are expected to exist in the Arctic region as well but ITWs with diurnal periods are not explicitly mentioned in their paper.

APPENDIX A: Effects of density stratification

The snapshots of horizontal velocity shown in Fig. A2 and Fig. A4 indicate that the distribution of the horizontal velocity coincide fairly well between Case 1 and Case 2, telling us that the effects of the density profile are negligible when temperature and salinity are held fixed.

(Case 1) When the isotherm and isohaline were taken along the constant sigma surfaces
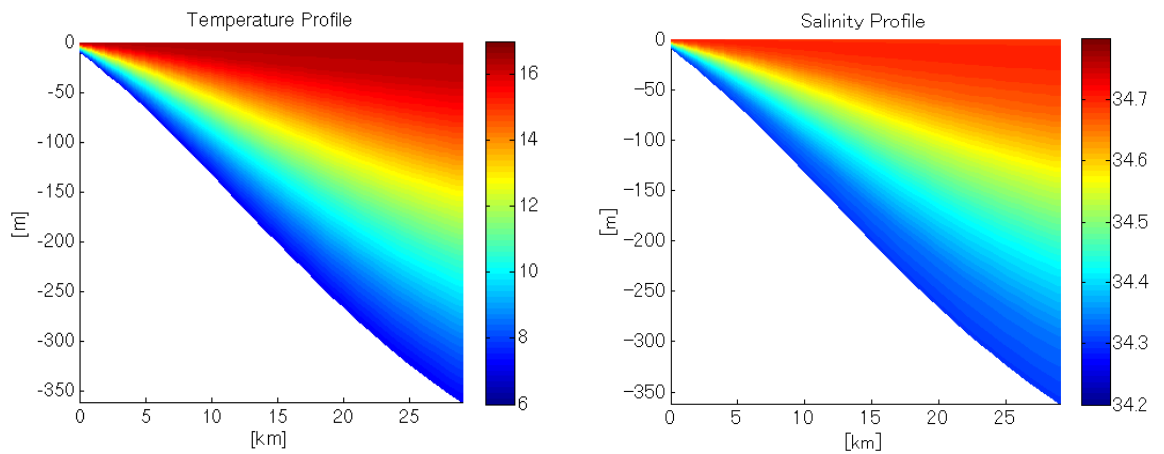

Figure A1. Profile of potential temperature and salinity in Celsius and psu respectively.
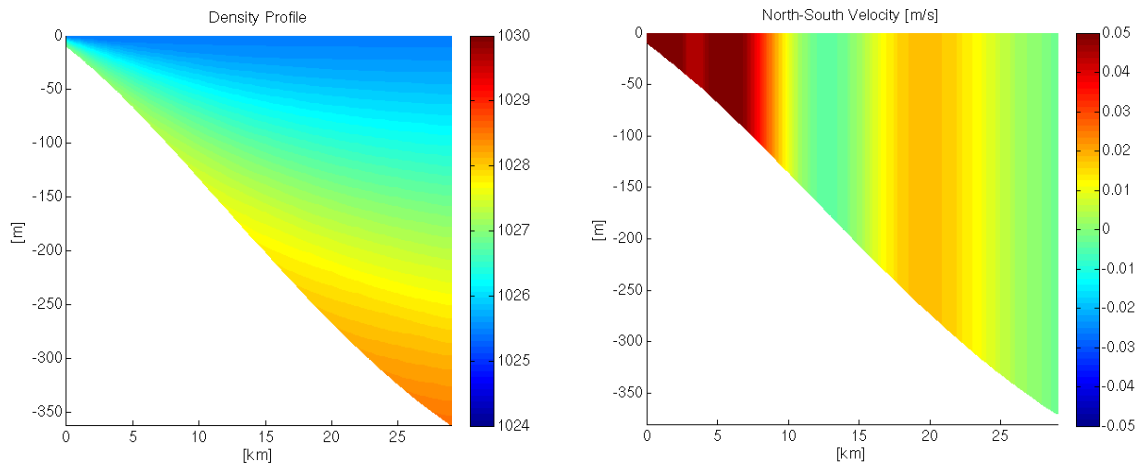
Figure A2. The density profile and a snapshot of north-south component of horizontal velocity at a certain time when there was no bottom friction.

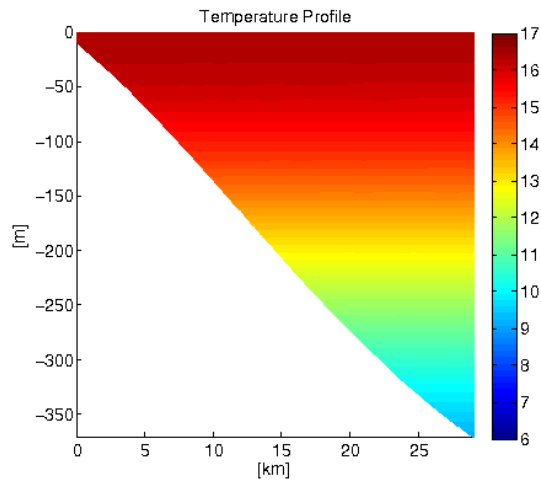(Case 2) When the isotherm was taken on the constant z surfaces and salinity was vertically constant

Figure A3. Profile of potential temperature in Celsius. Salinity was vertically uniform as 34.5 psu.
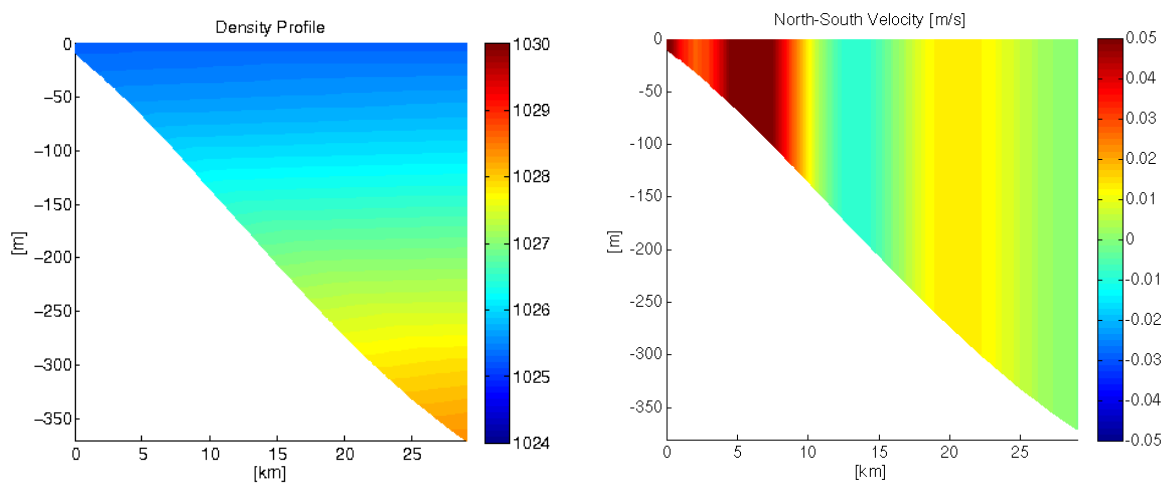
APPENDIX B: What is potential temperature?

Potential temperature is the temperature a fluid parcel would obtain if it were moved adiabatically to the sea surface, in other words, when the pressure were shifted adiabatically to atmospheric pressure. In order to convert in-situ temperature into potential temperature, we shall take a thermodynamic approach as treated by Gill[11] (1982). From the first law of thermodynamics, we obtain:

$$dU = Tds - PdV \tag{B1}$$

The term Tds represents the increase in heat content per unit mass of the fluid where s is a function of P and T and we shall define

$$c_P \equiv T\left(\frac{\partial s}{\partial T}\right)_P = \left(\frac{\partial U}{\partial T}\right)_P + P\left(\frac{\partial V}{\partial T}\right)_P$$

$$V \equiv \frac{1}{\rho} \text{ (: specific volume)} \tag{B2}$$

From equation (B1), we get

$$T\left(\frac{\partial s}{\partial P}\right)_T = \left(\frac{\partial U}{\partial P}\right)_T + P\left(\frac{\partial V}{\partial P}\right)_T \tag{B3}$$

and calculating, $\frac{\partial (B2)}{\partial P} - \frac{\partial (B3)}{\partial T}$:

$$\left(\frac{\partial s}{\partial P}\right)_T = -\left(\frac{\partial V}{\partial T}\right)_P \tag{B4}$$

Therefore, the total differentiation: $Tds = T\left(\frac{\partial s}{\partial T}\right)_P dT + T\left(\frac{\partial s}{\partial P}\right)_T dP$ can be written as

$$Tds = c_P dT - T\left(\frac{\partial V}{\partial T}\right)_P dP \tag{B5}$$

For isentropic change, equation (B5) can be rewritten as

$$dT = \frac{T}{c_P}\left(\frac{\partial V}{\partial T}\right)_{P,s} dP = -\frac{T}{\rho^2 c_P}\left(\frac{\partial \rho}{\partial T}\right)_{P,s} dP = \frac{\alpha T}{\rho c_P} dP \tag{B6}$$

where

$$\alpha \equiv -\frac{1}{\rho}\left(\frac{\partial \rho}{\partial T}\right)_{P,s}$$

Using the hydrostatic approximation, equation (B6) gives:

$$\Gamma = -\frac{dT}{dz} \equiv \frac{g\alpha T}{c_P} \tag{B7}$$

which is called the adiabatic elapse rate, and allows us to calculate

$$\Theta = T + \int_z^0 \Gamma\, dz \tag{B8}$$

APPENDIX C: Conversion of the governing equations from Cartesian coordinates to sigma coordinates

Only x and z dependencies will be considered; extension to the y coordinate is trivial. Permuting the coordinates as:

$$x = x^*, t = t^*, \sigma = \frac{z - \eta(x,t)}{D}; \ D = H(x) + \eta(x,t) \tag{C1}$$

where $\sigma = 0, -1$ at $z = \eta, -H$ respectively. Taking the x, z and t partial derivative of σ, we get

$$\frac{\partial \sigma}{\partial x} = \frac{\partial}{\partial x}\left(\frac{z - \eta(x,t)}{D}\right) = -\frac{z - \eta(x,t)}{D^2}\frac{\partial D}{\partial x} - \frac{1}{D}\frac{\partial \eta}{\partial x} = -\frac{1}{D}(\eta_x + \sigma D_x) \tag{C2a}$$

$$\frac{\partial \sigma}{\partial z} = \frac{\partial}{\partial z}\left(\frac{z - \eta(x,t)}{D}\right) = \frac{1}{D} \tag{C2b}$$

$$\frac{\partial \sigma}{\partial t} = -\frac{1}{D}(\eta_t + \sigma D_t) \tag{C2c}$$

From the continuity equation

$$\frac{\partial U}{\partial x} + \frac{\partial W}{\partial z} = 0 \tag{C3}$$

Using equation (C2a) and (C2b), we obtain:

$$\frac{\partial U^*}{\partial x^*}\frac{\partial x^*}{\partial x} + \frac{\partial U^*}{\partial \sigma}\frac{\partial \sigma}{\partial x} + \frac{\partial W^*}{\partial \sigma}\frac{\partial \sigma}{\partial z} = 0 \tag{C4}$$

$$\therefore \ \frac{\partial U^*}{\partial x^*} - \frac{\partial U^*}{\partial \sigma}\frac{1}{D}(\eta_x + \sigma D_x) + \frac{1}{D}\frac{\partial W^*}{\partial \sigma} = 0 \tag{C5}$$

Since

$$W = \frac{dz}{dt} = \frac{d}{dt}(\eta + \sigma D) \tag{C6}$$

$$\frac{d\eta}{dt} = \eta_t + U\eta_x \tag{C7}$$

$$\frac{d(\sigma D)}{dt} = \sigma_t D + \sigma D_t + U(\sigma_x D + \sigma D_x) + W\sigma_z D$$

$$= \frac{d\sigma}{dt} + U\sigma D_x + \sigma D_t \tag{C8}$$

equation (C6) ~ (C8) gives us:

$$\frac{\partial W}{\partial \sigma} = \frac{dw}{d\sigma} + \frac{dU}{d\sigma}(\sigma D_x + \eta_x) + UD_x + D_t; \ w = \frac{d\sigma}{dt} \tag{C9}$$

Plugging equation (B9) into (B5) after omitting the asterisk signs yields:

$$D\frac{dU}{dx} - \frac{\partial U}{\partial \sigma}(\eta_x + \sigma D_x) + \frac{\partial w}{\partial \sigma} + \frac{\partial U}{\partial \sigma}(\eta_x + \sigma D_x) + UD_x + D_t = 0$$

$$\therefore \ \frac{\partial}{\partial x}(UD) + \frac{\partial w}{\partial \sigma} + \frac{\partial \eta}{\partial t} = 0 \tag{C10}$$

which corresponds to equation (74).

For the momentum equation, including the Coriolis term is straight forward so neglecting it, we have

$$\frac{\partial U}{\partial t} + U\frac{\partial U}{\partial x} + W\frac{\partial U}{\partial z} = -\frac{1}{\rho_0}\frac{\partial P}{\partial x} + \frac{\partial}{\partial z}\left(\nu_V\frac{\partial U}{\partial z}\right) + F_x \qquad (C11)$$

where F_x represents the horizontal viscous terms. Using equation (C2a) ~ (C2c), the right-hand side and the pressure term on the left-hand side of equation (C11) can be written as:

$$\text{RHS} = \frac{\partial U^*}{\partial t^*} - \frac{\partial U^*}{\partial \sigma}\frac{1}{D}(\eta_t + \sigma D_t) + U^*\frac{\partial U}{\partial x^*} - U^*\frac{\partial U^*}{\partial \sigma}\frac{1}{D}(\eta_x + \sigma D_x)$$

$$+ \frac{1}{D}\{w + U^*(\sigma D_x + \eta_x) + \sigma D_t + \eta_t\}\frac{\partial U^*}{\partial \sigma}$$

$$= \frac{\partial U^*}{\partial t^*} + U^*\frac{\partial U^*}{\partial x^*} + \frac{w}{D}\frac{\partial U^*}{\partial \sigma} \qquad (C12)$$

$$\frac{\partial P}{\partial x} = \frac{\partial}{\partial x}\int_z^\eta \rho g\, dz = \rho(\eta)g\frac{\partial \eta}{\partial x} + \int_z^\eta \frac{\partial \rho}{\partial x} g\, dz$$

$$= \rho^*(0)g\frac{\partial \eta}{\partial x} + \int_\sigma^0 \left[\frac{\partial \rho^*}{\partial x^*} - \frac{\partial \rho^*}{\partial \sigma}\frac{1}{D}(\eta_x + \sigma D_x)\right]g\frac{\partial z}{\partial \sigma}d\sigma$$

$$= \rho^*(0)g\frac{\partial \eta}{\partial x} + \int_\sigma^0 \left[D\frac{\partial \rho^*}{\partial x^*} - \frac{\partial \rho^*}{\partial \sigma}(\eta_x + \sigma D_x)\right]g\, d\sigma$$

$$= \rho^*(0)g\frac{\partial \eta}{\partial x} + g\int_\sigma^0 \left[D\frac{\partial \rho^*}{\partial x^*} - \sigma D_x\frac{\partial \rho^*}{\partial \sigma}\right]d\sigma - \left(\rho^*(0) - \rho^*(\sigma)\right)g\frac{\partial \eta}{\partial x}$$

$$= \rho^*(\sigma)g\frac{\partial \eta}{\partial x} + g\int_\sigma^0 \left[D\frac{\partial \rho^*}{\partial x^*} - \sigma D_x\frac{\partial \rho^*}{\partial \sigma}\right]d\sigma \qquad (C13)$$

After omitting the asterisks and substituting equation (C12) and (C13) into equation (C11) yields:

$$\frac{\partial U}{\partial t} + U\frac{\partial U}{\partial x} + \frac{w}{D}\frac{\partial U}{\partial \sigma} + g\frac{\partial \eta}{\partial x} = -\frac{g}{\rho_0}\int_\sigma^0 \left[D\frac{\partial \rho}{\partial x} - \sigma D_x\frac{\partial \rho}{\partial \sigma}\right]d\sigma + \frac{1}{D}\frac{\partial}{\partial \sigma}\left[\frac{\nu_V}{D}\frac{\partial U}{\partial \sigma}\right] + F_x$$

$$\therefore D\frac{\partial U}{\partial t} + UD\frac{\partial U}{\partial x} + w\frac{\partial U}{\partial \sigma} + gD\frac{\partial \eta}{\partial x}$$

$$= -\frac{gD^2}{\rho_0}\int_\sigma^0 \left[\frac{\partial \rho}{\partial x} - \frac{\sigma}{D}\frac{\partial D}{\partial x}\frac{\partial \rho}{\partial \sigma}\right]d\sigma + \frac{\partial}{\partial \sigma}\left[\frac{\nu_V}{D}\frac{\partial U}{\partial \sigma}\right] + F_x \qquad (C14)$$

Using the relation $D_t = \eta_t$, $U \times$ (B10) + (B14) gives:

$$\frac{\partial(UD)}{\partial t} + \frac{\partial(U^2 D)}{\partial x} + \frac{\partial(Uw)}{\partial \sigma} + gD\frac{\partial \eta}{\partial x} + \frac{gD^2}{\rho_0}\int_\sigma^0 \left[\frac{\partial \rho}{\partial x} - \frac{\sigma}{D}\frac{\partial D}{\partial x}\frac{\partial \rho}{\partial \sigma}\right]d\sigma$$

$$= \frac{\partial}{\partial \sigma}\left[\frac{\nu_V}{D}\frac{\partial U}{\partial \sigma}\right] + F_x \qquad (C15)$$

which corresponds to equation (75) without the Coriolis term. The energy equations can be derived in the same manner.

APPENDIX D: Forced oscillation of a spring

First, let us consider the case when there is no friction:

$$m\ddot{x} = -k(x - a\cos\omega t) \tag{D1}$$

where a and ω are the amplitude and frequency of the forcing respectively. Placing $F_0 = ka$, $\sigma_0^2 = k/m$, we get

$$\ddot{x} + \sigma_0^2 x = \frac{F_0}{m}\cos\omega t \tag{D2}$$

Solution for the homogenous equation is

$$x = A\cos\sigma_0 t + B\sin\sigma_0 t \tag{D3}$$

In deriving the particular solution of equation (D1), we shall rewrite (D1) as

$$\ddot{x} + \sigma_0^2 x = \frac{F_0}{m}e^{i\omega t} \tag{D4}$$

and assume a solution in shape of $x^* = Ce^{i\omega t}$. Plugging this into the equation above, we get:

$$C_1 = \frac{F_0/m}{\sigma_0^2 - \omega^2} \tag{D5}$$

Therefore, taking the real part, we have

$$x = A\cos\sigma_0 t + B\sin\sigma_0 t + \frac{F_0/m}{\sigma_0^2 - \omega^2}\cos\omega t \tag{D6}$$

Since the dominator of D_1 reaches a maximum at $\omega = \omega_1 = \sigma_0$, a resonance occurs when this condition is satisfied. Now, when friction exists, the equation can be written as:

$$m\ddot{x} = -kx + ka\cos\omega t - \tau\dot{x}$$

$$\therefore \ \ddot{x} + 2\gamma\dot{x} + \sigma_0^2 x = \frac{F_0}{m}\cos\omega t \tag{D7}$$

where τ is the friction factor and $\gamma = \tau/2m$. When friction is small i.e.) $\gamma < \sigma_0$, the solution for the homogenous solution is:

$$x = Ae^{-\gamma t}\cos\sqrt{\sigma_0^2 - \gamma^2}t \tag{D8}$$

Taking the same steps when there was no friction, we have the particular solution:

$$x^* = C_2\cos(\omega t + \varphi) \tag{D9}$$

where

$$C_2 = \frac{F_0/m}{\sqrt{(\sigma_0^2 - \omega^2)^2 + 4\gamma^2\omega^2}}$$

and the solution for (D2) can be written as:

$$x = Ae^{-\gamma t}\cos\sqrt{\sigma_0^2 - \gamma^2}t + \frac{F_0/m}{\sqrt{(\sigma_0^2 - \omega^2)^2 + 4\gamma^2\omega^2}}\cos(\omega t + \varphi) \tag{D10}$$

When $\gamma < \sigma_0/\sqrt{2}$ $(= \tau < \sqrt{2mk})$, the dominator of D_2 takes a maximum value when

$$\omega = \omega_2 = \sqrt{\sigma_0^2 - 2\gamma^2} \qquad (D11)$$

We see that $\omega_1 > \omega_2$, hence $T_1 < T_2$, meaning that the resonant periods lengthen when friction exists.

REFERENCES

[1] Longuet-Higgins M. S. (1969) On the trapping of long-period waves round islands. *J. Fluid Mech.*, 37, 773-784.

[2] Longuet-Higgins M. S. (1970) Steady currents induced by oscillations round islands. *J. Fluid Mech.*, 42, 701-720.

[3] Longuet-Higgins M. S. (1971) On the spectrum of sea level at Oahu. *J. Geophys. Res.*, 76, 3517-3522

[4] Wunsch C. (1972) The spectrum from two years to two minutes of temperature fluctuations in the main thermocline at Bermuda. *Deep-sea Res.*, 19, 577-593.

[5] Hogg N. G. (1980) Observations of Internal Kelvin Waves Trapped round Bermuda. *J. Phys. Oceanogr.*, 10, 1353-1376.

[6] Brink K. H. (1999) Island-trapped waves, with application to observations off Bermuda. *Dyn. Atmos. Ocean*, 29, 93-118.

[7] Ohwaki A., Matsuyama M. and Nagashima H. (1994) Difference in the Prevailing Periods of Internal Tides between Sagami and Suruga Bays: Numerical Experiment. *J. Oceanogr.*, 50, 449-463.

[8] Ohwaki A., Matsuyama M. and Iwata S. (1991) Evidence for Predominance of Internal Tidal Currents in Sagami and Suruga Bays. *J. Oceanogr. Soc. Japan*, 47, 194-206.

[9] Mellor G. L. (1991) Introduction to Physical Oceanography. *AIP Press*, 114-115.

[10] Mellor G. L. (2004) User's Guide for A Three-Dimensional, Primitive Equation, Numerical Ocean Model. http://www.aos.princeton.edu/WWWPUBLIC/htdocs.pom/.

[11] Gill A. E. (1982) Atmosphere-Ocean Dynamics. *Academic Press*, 50-51.

[12] Clarke A. J. (1977) Observational and Numerical Evidence for Wind-Forced Coastal Trapped Long Waves. *J. Phys. Oceanogr.*, 7, 231-247.

[13] Huthnance J. M. (1978) On Coastal Trapped Waves: Analysis and Numerical Calculation by Inverse Iteration. *J. Phys. Oceanogr.*, 8, 74-92.

[14] Miyata M. and Groves G. W. (1968) Note on Sea Level Observations at Two Nearby Stations. *J. Geophys. Res.*, 73, 3965- 3967.

[15] Miyata M. (1993) Island-trapped shelf waves. *La mer*, 31, 169-178.

[16] Kowalik Z. and Stabeno P. (1999) Trapped motion around the Pribilof Islands in the Bering Sea. *J. Geophys. Res.*, 104, 25667-25684.

[17] Kowalik Z. and Proshutinsky A. Y. (1995) Topographic enhancement of tidal motion in the western Barents Sea. *J. Geophys. Res.*, 100, 2613-2637.

[18] Jordi A. and Wang D. P. (2012) sbPOM: A parallel implementation of Princeton Ocean Model. *Env. Mod. & Soft.*, 38, 59-61.

[19] Sil S., Miyazawa Y., Varlamov S. M., Miyama T., Waseda T. and Guo X. (2013) Topography-tide-current interaction on the South of the Japan. *IWMO*. Yokohama, Japan.